CHALMERS
UNIVERSITY OF TECHNOLOGY

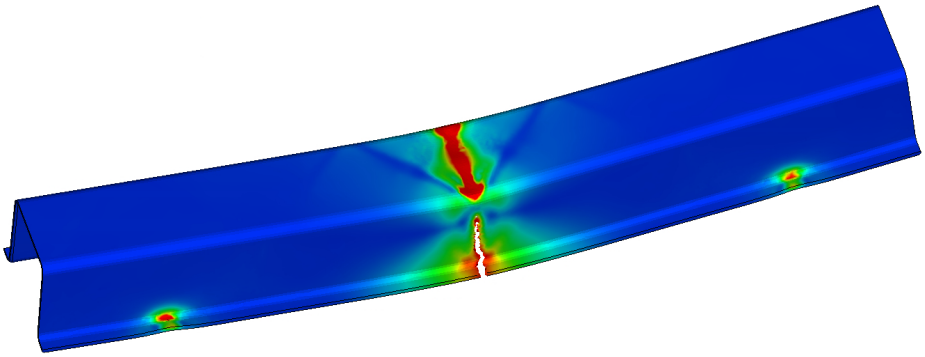

CAE Modeling of HPDC Aluminum

A Correlation Study on Material Properties and Simulation Accuracy through experimental validation on a component level

Master's thesis in Applied Mechanics

LUKAS LARSSON
MELVIN JOHANSSON

DEPARTMENT OF INDUSTRIAL AND MATERIALS SCIENCES

CHALMERS UNIVERSITY OF TECHNOLOGY
Gothenburg, Sweden 2025
www.chalmers.se

Master's thesis 2025

CAE Modeling and Correlation of HPDC Aluminum

A Correlation Study on Material Properties and Simulation Accuracy through experimental validation on a component level

LUKAS LARSSON
MELVIN JOHANSSON

CHALMERS
UNIVERSITY OF TECHNOLOGY

Department of Industrial and Materials Sciences
Chalmers University of Technology
Gothenburg, Sweden 2025

CAE Modeling and Correlation of HPDC Aluminum
A Correlation Study on Material Properties and Simulation Accuracy through experimental validation on a component level
LUKAS LARSSON
MELVIN JOHANSSON

Supervisor: Adj. Prof. Renaud Gutkin, Volvo Car Corporation, Department of Industrial and Materials Science, Chalmers University of Technology.
Examiner: Prof. Magnus Ekh, Department of Industrial and Materials sciences

Master's Thesis 2025
Department of Industrial and Materials Science
Chalmers University of Technology
SE-412 96 Gothenburg
Telephone +46 31 772 1000

Cover: Strain field in a beam subjected to three point bending (visualization made with Meta Post-processor).

Typeset in LaTeX
Gothenburg, Sweden 2025

CAE Modeling of HPDC Aluminum
A Correlation Study on Material Properties and Simulation Accuracy through experimental validation on a component level
LUKAS LARSSON, MELVIN JOHANSSON
Department of Industrial and Materials Sciences
Chalmers University of Technology

Abstract

This thesis seeks to improve the correlation between the results of physical testing and simulations for a HPDC aluminum component loaded until failure. Physical experimental data was gathered through a three point bending test of cast beams and further validated with tensile tests using coupons from the same casting component. Explicit time-stepping simulations were carried out using LS-DYNA and failure models GISSMO and CrachFEM were used for solid and shell elements. Analysis from physical test results revealed the need to incorporate porosity into the model, both through pore meshing and scaling on different levels. Scaling was justified with representative volume elements. Quantitative improvements were made, significantly reducing error. Two different macro-mapping methods reduced the error both in peak force, displacement at failure and absorbed energy. Error went from 66.2%(force), 25.0%(displacement) and 77.3%(energy) to 7.70% & 7.74% (force), 12.5% & 31.28%(displacement) and 12.5% & 46.97% (energy).

Additionally, time for meshing with hexahedral elements was reduced from one week to mere minutes, while maintaining accuracy comparable to tetra elements. This method shows promise for reducing shear locking. The study found no major differences between first and second order solid elements for both tetrahedral and hexahedral meshes other than computational cost. The micro-mapping methodology developed in this investigation using CT-scan data and casting process simulation data proved insufficient in accounting for the disparities between experiment and simulation results and needs further development. The thesis also explores the potential of Isogeometric Analysis (IGA) as a future method, noting its current limitations and immaturity for practical application.

Furthermore, the study investigated alloys with increased iron and vanadium content, imitating the use of recycled material, to determine if there were any significant differences between them. However, no clear differences were observed, which may be attributed to larger sources of error overshadowing the potential variations between the alloys.

Keywords: HPDC, Aluminum, CAE Correlation, Mapping, Representative volume elements (RVE), Isogeometric Analysis (IGA)

Acknowledgements

We would like to express our sincere gratitude to Volvo Cars and especially Renaud Gutkin for giving us the opportunity to work on this project, providing excellent ideas, and offering great feedback. Our supervisors Per-Anders Eggertsen and Johan Jergeus deserve special thanks for sharing their extensive knowledge on material models, failure prediction and simulations in DYNA and supporting us during the project. Mats Landervik was instrumental in providing scripts for the mapping process and guiding us through it. Anton Hvitt Hultmark offered valuable insights into the casting process and qualitative post-processing of test results. We appreciate the contributions of Jihui and Nithin for providing tensile test data. We want to thank Kübra Yavuz Yılmaz for supplying useful data from cast simulations in ProCast and Stephan Esteki's assistance with CT scanning, without which mapping would not have been possible. Huge thanks to Milton Pena Aza at BETA for help with hexahedral meshing and Amir Riazi for his assistance with CAE IT support.

We are also grateful to David Johansson for making the testing possible, and Robert Olsson for his assistance in preparing the test specimens, and to Richard Sandberg for helping set up the test rig. Johann Körbelin contributed significantly to the gathering of test results, assisting with setting up force monitoring and Digital Image Correlation (DIC) as well as post-processing of DIC-data.

Additional thanks to the entire CAE team at Safety and Durability center for welcoming us and making us feel part of the team, and our good friend Bilal Siddiqui for the many laughs we shared over lunch.

We would also like to express our sincere gratitude to Stefan Zoric for his thorough feedback and for serving as opposition to our thesis, providing us a fresh perspective on our work. Finally, we would like to extend our heartfelt thanks to our examiner Magnus Ekh for guidance, support, and valuable feedback throughout the course of this thesis.

Lukas Larsson & Melvin Johansson, Gothenburg, June 2025

List of Acronyms

Below is the list of acronyms that have been used throughout this thesis listed in alphabetical order:

3pb	Three point bend
BIW	Body In White
CAE	Computer Aided Engineering
cc	center to center
CTM	CT-scan based Mapping
CT-scan	Computer Tomography scan
DIC	Digital Image Correlation
EEL	Element Edge Length
EL	Element
ELFORM	Element Formulation
Fe	Iron
FEA	Finite Element Analysis
FEM	Finite Element Method
GenYld	Generalized Yield
GISSMO	General Incremental Stress State dependent damage MOdel
GTN	Gurson-Tvergaard-Needleman
HPDC	High Pressure Die Casting
IGA	Isogeometric Analysis
LAP	Load Angle Parameter
MF	Material Formulation
NDT	Non-Destructive Testing
PID	Part ID
PSDM	Process Simulation Data based Mapping
RBF	Radial Basis Function
RVE	Representative Volume Elements
V	Vanadium
VCC	Volvo Cars Corporation

Contents

1
Introduction

Cast aluminium is widely used in automotive applications but the mechanical properties of such components are highly dependent on the manufacturing process, which can introduce imperfections eg. porosity. Imperfections such as these have a significant influence on the material response and fracture behavior and are notoriously hard to predict. Preliminary studies have indicated significant variations in material properties in relation to process parameters such as flow length and cooling time that impact elongation at failure and ultimate strength [1]. This thesis proposal was brought forward by Volvo Cars, in order to investigate the potential for modeling new parts to be cast in aluminium and accurately capturing behaviors for the purpose of ensuring vehicle safety performance.

Aluminium is lightweight (about a third of the density of steel), strong, and ductile and exhibits good castability, making it a suitable alternative to steel for automotive components [7]. The use of cast aluminium in automotive applications is also becoming more attractive as the automotive industry is undergoing electrification. Lightweight components lead to longer range and higher efficiency, which have economic and environmental incentives. Volvo has therefore initiated research into aluminium megacasting, in this case part of the floor in the body in white (BIW). Casting offers significant reduction in geometric complexity of components thus also leading to easier production. The process of megacasting parts in aluminium also supports the incorporation of more recycled materials, aiming for a circular system in which Volvo in the future can reclaim and recycle their own vehicles, thus opening up the door for reduced emissions and enhanced sustainability.

However, recycled material, and casting in general, reduces the reliability of the part due to uncertainties in material behavior and increased amount of imperfections. Being able to ensure safety and durability becomes a major concern, hence the need to investigate material response in crash tests. Modern techniques for doing so have come to rely increasingly on numerical modeling, primarily due to the economic and time benefits. For this, it is essential that appropriate methods are implemented in order to accurately model the behavior of the part and its material, in this case using commercial finite element analysis (FEA) software. It is also known that replacing steel parts with aluminium cannot be done via simple substitution, rather it requires a redesign of the part itself, adjacent parts and subsequently a redesign of the production process chain [8]. This further emphasizes the need for being able to accurately model the part and produce a so-called 'digital twin'.

Many numerical tools exist and are used for modeling the behavior of components. Specifically the pre-processing tool Ansa and the FEM solver LS-Dyna are used by Volvo cars together with material models for failure and fracture, namely MFGenYld, CrachFem and GISSMO (General Incremental Stress State dependent damage MOdel) [25][26]. In order to validate and calibrate the models, physical tests are performed on components. For this purpose, a so called 'snake-tool' has been developed to imitate real cast parts of difficult geometries. The role of the 'snake-tool' is, in other words, to emulate the behavior of cast components but is simpler and cheaper to cast than the actual components.

Figure 1.1: Mega-cast part

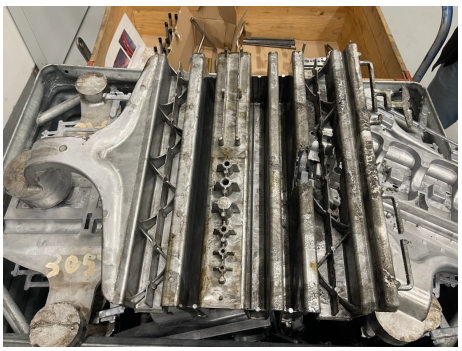

Figure 1.2: Snake-tool, first cast

There have been a few theses conducted for Volvo Cars on the material behavior of cast aluminium, including the aforementioned study of pore geometry by Coric and Seyedraoufi [1] that used X-ray tomography along with Representative Volume Elements (RVE) and FEM to study how pore shape, volume and distribution affected the strength and ductility of aluminium. Further, Shreedhara and Singh [2] worked on correlating physical drop tests to modeled test rigs and found that using the material and failure models MFGenYld and CrachFEM showed the better correlation with solid elements than shell elements but were very mesh dependent, and concluded mass scaling had no significant impact on accuracy but decreased simulation time. Lastly Al-Karawi and Mathiesen [3] further compared shell and solid elements in crash simulations using material coupons comparing also the material failure model GISSMO to CrachFEM and concluded that the latter is extremely limited in solid element modelling and that the prior might be more suitable for this element type.

The following sections present the objective and the delimitations. The report then goes on to present relevant theory followed by the method, results and lastly a discussion. The report assumes a baseline knowledge of mechanics of solids and specifically finite element analysis.

1.1 Objective

The goal of this thesis is to perform a correlation study of the existing material and fracture models of cast aluminium by comparing numerical models to physical testing of cast components. The purpose of the investigation therefore raises the following objectives:

- *Construct a test rig and perform a three point bending test in order to investigate the physical response of the material on a component level*
- *Investigate the extent that presence of recycled material and increased levels of iron and vanadium affect material properties when tested on a component level*
- *Construct a CAE model to represent and simulate the physical test with the finite element model*
- *Study existing material models in combination with element formulations and conclude which of these that are best suited for accurately and efficiently modeling this system*
- *Integrate process related properties such as porosity into the model and conclude on the extent at which they improve the accuracy of the simulations*
- *Investigate whether simulation time can be reduced by implementation of Isogeometric analysis (IGA) and the extent of which accuracy is impacted*

1.2 Delimitations

To limit the scope of the project, it is important to note that the purpose of this investigation is not to answer to what degree the cast part could reduce production complexity, nor to what degree it could enhance sustainability, nor how casting impacts the structural integrity of the part. Instead, this investigation aims to answer the question of "to what extent can the cast aluminium in different regions of the part with different levels of recycled metal be modeled?", and "which parameters are most influential when it comes to strength and failure?". Thus, no physical tests will be done on the actual part rather a "snake tool" will be modeled and tested.

It may also be relevant to note that the investigation does not aim to design any new FEM code, rather, state of the art commercial FEM software such as ANSA, LS-Dyna and Meta, will be employed to set up and simulate the model and post-process the results respectively.

Regarding the actual testing, an important delimitation is that a quasi-static assumption is made, meaning strain-rate dependent effects are ignored. This is due to the time limitation of the project, the complexity and expense of performing strain rate tests and lastly that it is a relatively valid assumption to make about aluminium specifically since it has shown lower strain-rate dependent effects compared to steels

[9]. The consequence of this is that the physical tests will be carried out at a slow load rate and it will be assumed that the material will in general behave the same way at a much faster load rate, such as that of a crash.

2

Theory

The following chapters regard the theory necessary to understand the basis of the project and assumes a fundamental understanding of continuum and material mechanics. The topics covered here are how yield criteria can be modeled, how principal stresses can be transformed into a triaxiality-Lode angle coordinate system, three of the most common failure types, an introduction to the material and failure models MFGenYld, CrachFEM and GISSMO as well as relevant information needed to understand the FEM solvers themselves regarding element types and implicit/explicit time-stepping.

2.1 Material yielding and hardening

Since this project regards safety and durability, it is highly relevant to model material until failure and therefore it is prudent to have an understanding of the yielding criteria that the models use and also make an important distinction between material models and failure models. This is because some models strictly handle material behavior in the linear elastic region where a linear relationship between stress and strain takes place such as *MAT_24* developed by *LSTC* [16]. Others strictly handle failure, such as *GISSMO* developed by *DYNAmore* or *CrachFEM* developed by *MATFEM*, that need to be coupled with material models. In this thesis all these models are simulated using *LS-DYNA* also developed by *LSTC*.

A material subjected to a load begins to deform under the presence of stress. With enough stress and deformation a material is said to yield, where irreversible deformation develops. A yield criteria is defined based on the stress state of the material and since stress is a second order tensor, the yield for an isotropic material is a function of the principal stresses $\sigma_1, \sigma_2, \sigma_3$ and so yield surfaces also known as yield loci can be visualized as in Figure 2.1. The material model *MAT_24* uses the well known *von Mises* criterion.

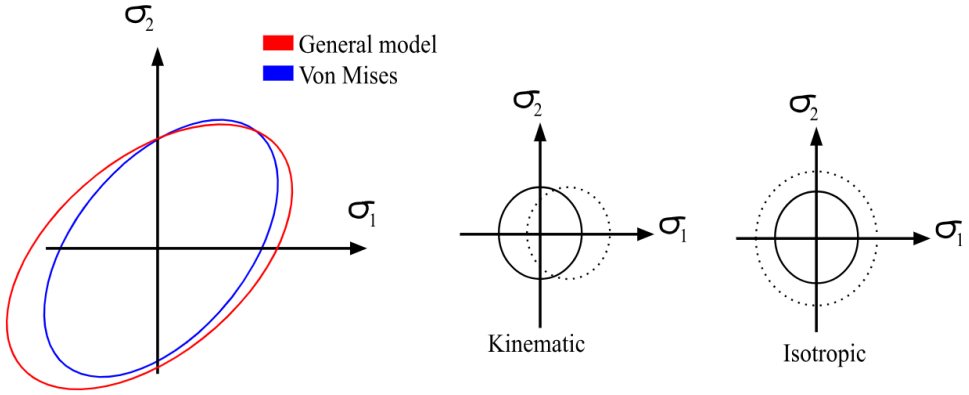

Figure 2.1: Yield loci for Tresca, Von Mises, Kinematic and Isotropic hardening

Upon yielding, plastic strain initiates, leading to hardening of the material. Figure 2.2 illustrates the non-linear strain-stress relationship, highlighting the plastic deformation region where permanent deformation persists after unloading. Two very common forms of hardening are isotropic and kinematic hardening as shown in Figure 2.1. In isotropic hardening, a material's new yield strength is equally expanded in every axis in the principal stress plane, while kinematic hardening is a translation of the yield loci in the direction of the loading. In other words, the shift of the yield locus in kinematic hardening, leads to a material reaching plasticity sooner for reversed compressive loading. An important characteristic of the *MFGenYld* material model (also developed by *MATFEM*) is that it is isotropic but the yield locus shape can be generalized [25]. This generalization means that the material properties can be tailor made and therefore more sophisticated than *MAT_24*. The non-linearity after yielding is modeled depending on the so called material card that is calibrated for specific alloys, plastics, etc.

For simulating the non-linear plastic region, the two main approaches are either to tabularize the hardening curve or to use a function, both of which are calibrated from physical testing. Figure 2.2 showcases 5 different hardening curves for the material models used in this investigation. The tabular data is likely produced by material model functions, but the functions themselves are not openly shown as it can be considered intellectual property. The physical testing used for the calibration includes a range of quasi-static tests such as tensile tests, notched tensile tests, shear tests, punch tests, plate bending, round tensile tests, etc. These tests are performed and used to calibrate material parameters (in this case a,b,c,d,e,f,g,h) used for the approximation of the hardening response. There are many such hardening models but relevant for this investigation is the Hocket-Sherby model (Eq. 2.1) and the modified Ghosh model (Eq. 2.2). In the elastic region, stress and strain are related by Young's modulus, expressed as $\sigma = E\varepsilon$. However, in the non-linear region, yield stress 'σ_Y' depends on the plastic strain (ε_p), which explains why $\sigma_Y(\varepsilon_p = 0) \neq 0$ in the figure.

$$\sigma_Y(\varepsilon_p) = a - b * \exp(-c * \varepsilon_p^d) \tag{2.1}$$

$$\sigma_Y(\varepsilon_p) = e(f + \varepsilon_p)^g - h \tag{2.2}$$

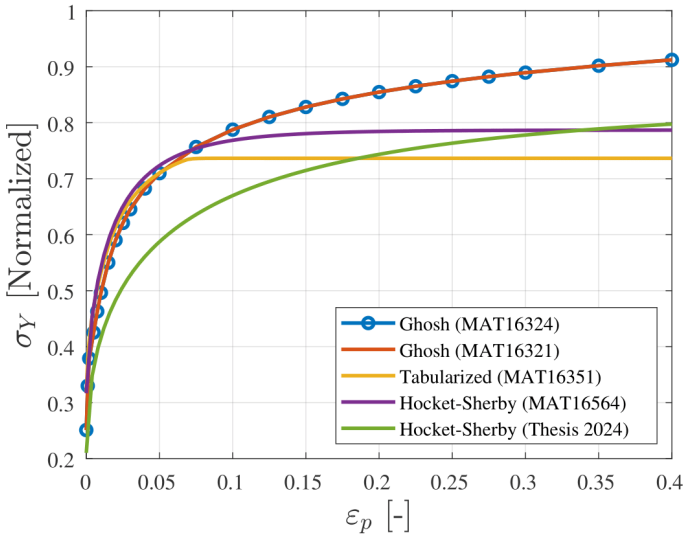

Figure 2.2: Flow stress curves for the material cards used in this investigation

The hardening response defines how stiffly a component will react to stress and as can be seen from Figure 2.2 even though all of these have been calibrated for the same material, they still differ quite significantly. This is most probably because the samples that were used for calibration were taken from different locations in the cast component. These stiffness of the material will ultimately decide how much load a component can bear before it fails.

2.2 Element types and formulations

The types of elements used in the simulations are solid- and shell elements. For the shell elements, both triangular and quadrilateral elements are used. In this investigation *LS-Dyna* is used as a solver where element formulations are denoted as ELFORMX and are used to refer to for example element type, local degrees of freedom, shape function polynomial order, number of integration points, number of midpoints, etc. For shells ELFORM16 is used, while ELFORM13 is used for tetrahedral solids and ELFORM-1 is used for hexahedral solids.

2.2.1 Hexahedral element formulations

ELFORM-1 (minus 1) is a commonly used formulation for eight noded hexahedral elements, efficient for poor aspect ratios. This formulation is said to be 'fully integrated', with 8 Gaussian integration points, as opposed to under-integrated where only one Gauss point is used, where there is a tradeoff between accuracy and computational cost. Fully integrated elements can also suffer from shear locking due to problems with realizing bending modes without also introducing strain [16].

2.2.2 Tetrahedral element formulations

ELFORM10 is the element formulation for a four noded tetrahedral element with a single integration point and linear basis functions [12]. It is in this sense one of the most simple solid elements, however, it is considered too stiff to give reliable results which is why ELFORM13 is preferred for tetrahedral elements. ELFORM13 is also known as a one point nodal pressure tetrahedron where in the element routine, the volumetric strain is averaged over adjacent elements to "smooth the pressure response". This is to alleviate the phenomena known as volumetric locking, and while it is more common occurance among incompressible materials where Poisson's ratio is close to 0.5, it is present also for materials showing large plastic strains (and small elastic) which can be true for ductile failure of aluminium. Unfortunately for this investigation, while ELFORM13 is considered more accurate, it is not compatible with strain and hardening mappings in the current version of the simulation software (LS-DYNA) and so ELFORM10 has to be implemented for integration of process parameters (see chapter 2.8). To be clear, for simulations without mapping, ELFORM13 is used, and for those with mapping ELFORM10 is used. Lastly, ELFORM16 is a 5-point selectively integrated tetrahedral element with 10 nodes and quadratic basis functions. Increasing the number of integration points from one to five could increase the computational time of up to five times. Although this means that it takes much longer to run, it is of interest to see whether the higher order formulations are justified by their increased accuracy.

The use of second order tetrahedral elements in LS-Dyna is straightforward: take a first order tetrahedral mesh, change the element formulation to 16 or 17, and add the option *TET4TOTET10* which transforms the 4-noded first order tetra elements to 10-noded second order elements. While higher order elements can increase the accuracy of the finite element analysis, they may also predict unrealistic results, such as infinite stress at stress concentrations. These results are not physically representative, highlighting the need for careful interpretation.

2.2.3 Shell element formulations

Element formulation 16 is a shell element based on the Mindlin-Reissner kinematic assumption that normals remain perpendicular to the mid-surface after deformation. To avoid confusion, note that both solids and shells can each implement a so called ELFORM16 but these are completely different. It uses 2 by 2 integration points in the plane and throughout the simulations the number of through-thickness integration points is 5 (in total 20 integration points). It is the least computationally expensive of the 2×2 integrated shell elements available in LS-DYNA, but is 2-3 times more expensive than the Belytschko-Tsay shell element. The increased number of integration points from the Belytschko-Tsay element is beneficial however since it reduces the risk of hourglassing which can be an issue for under-integrated elements. Hour-glassing is essentially when elements deform in a non-physical way that looks a bit like hourglasses, and causes elements to exhibit less stiffness than expected.

2.3 Haigh-Westergaard Stress Space (Triaxiality and Lode)

Upon loading a material beyond its yield limit, it begins to plastically deform and after a given plastic strain the component fails and this is usually denoted as ε_{pf}. In the strain state space, the failure strain is path dependent which means that the deformation history of the element/component is needed to predict when it breaks. However, in the stress state space it is path independent meaning only the *current* stress state is needed to evaluate if failure criteria are met [23]. Figure 2.3 illustrates this point of using stress-state based failure models rather than strain history failure models where p_1 and p_2 are unique loading histories. The point to make here is that for stress-based failure models, one only needs to know the *current* stress to know if failure occurred, not the history of the stress and in general the *current* strain is not enough to know whether failure has occurred.

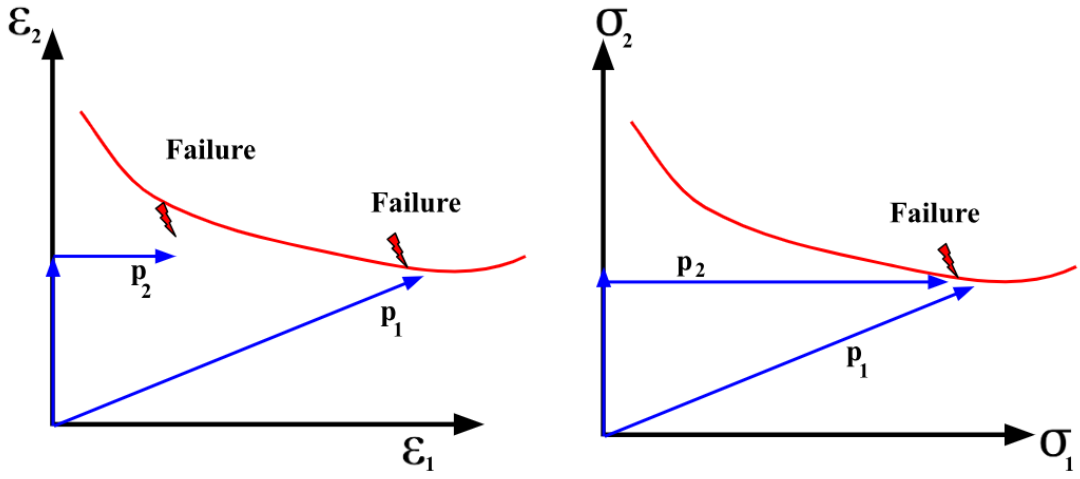

Figure 2.3: Principal stress and strain failure curves

Often the deviatoric and hydrostatic stress (Eq. 2.3) are used to define stress invariants (Eq. 2.4 and 2.5). These invarianets are in turn used to define the triaxiality (η) and the Lode angle parameter ($\bar{\theta}$) that make up the Haigh-Westergaard stress space. This is the stress space that the failure models CrachFEM and GISSMO use. Triaxiality (Eq. 2.6) is the ratio of the hydrostatic stress and the equivalent von Mises stress. It is an important measure since ductile failure stems from void nucleation, growth and coalescence in the material, and a high hydrostatic stress (positive) is physically analogous to expanding voids, increasing their size until so much damage is obtained that failure occurs. The normalized third stress invariant denoted ξ (Eq. 2.7) is a way of measuring the ratio between normal stress and deviatoric stress. From this the Lode angle is defined as θ (Eq. 2.8) while its normalized form is used to define the Lode angle parameter $\bar{\theta}$ (Eq. 2.9). Be aware that ξ, θ and $\bar{\theta}$ are often all referred to simply as 'Lode', but in this investigation they are referred to as the normalization of the third deviatoric stress invariant, the Lode angle and

the Lode angle parameter (LAP) respectively. The following derivations were taken from[26].

$$\boldsymbol{\sigma_{xyz}} = \begin{pmatrix} \sigma_{xx} & \tau_{xy} & \tau_{xz} \\ \tau_{yx} & \sigma_{yy} & \tau_{yz} \\ \tau_{zx} & \tau_{zy} & \sigma_{zz} \end{pmatrix}, \qquad \sigma_h = \frac{\sigma_{xx} + \sigma_{yy} + \sigma_{zz}}{3}, \qquad \boldsymbol{\sigma_d} = \boldsymbol{\sigma_{xyz}} - \boldsymbol{I}\sigma_h \tag{2.3}$$

$$\begin{aligned} I_1 &= \mathrm{tr}(\boldsymbol{\sigma}) = \sigma_{xx} + \sigma_{yy} + \sigma_{zz} \\ I_2 &= \frac{1}{2}\left[(\mathrm{tr}(\boldsymbol{\sigma}))^2 - \mathrm{tr}(\boldsymbol{\sigma}^2)\right] \\ I_3 &= \det(\boldsymbol{\sigma}) \end{aligned} \tag{2.4}$$

$$\begin{aligned} J_1 &= 0 \\ J_2 &= \frac{1}{3}\left[(\sigma_{xx} - \sigma_{yy})^2 + (\sigma_{yy} - \sigma_{zz})^2 + (\sigma_{zz} - \sigma_{xx})^2 + 6(\sigma_{xy}^2 + \sigma_{yz}^2 + \sigma_{xz}^2)\right] \\ J_3 &= \det(\boldsymbol{\sigma}_d) \end{aligned} \tag{2.5}$$

The von Mises yield criteria can now be expressed by defining the effective stress σ_{vM} as the second invariant to the deviatoric stress matrix: $\sigma_{vM} = \sqrt{3J_2}$. The invariants are then used to define triaxiality and Lode angle parameter as follows:

$$\eta = \frac{\sigma_h}{\sigma_{vM}} = \frac{I_1}{3\sqrt{3J_2}} \tag{2.6}$$

$$\xi = \frac{27}{2}\frac{J_3}{\sigma_h^3} \tag{2.7}$$

$$\theta = \frac{1}{3}cos^{-1}(\xi) \tag{2.8}$$

$$\bar{\theta} = 1 - \frac{6\theta}{pi} = 1 - \frac{2}{\pi}arccos(\xi) \tag{2.9}$$

The transformation that takes place to get the Haigh-Westergaard space is thus: $\{\sigma_1, \sigma_2, \sigma_3\} \Rightarrow \{\eta, \bar{\theta}, \sigma_{vM}\}$.

$$\begin{aligned} \sigma_1 &= \sigma_{vM}\left(\eta + \frac{2}{3}cos[\frac{\pi}{6}(1 - \bar{\theta})]\right) \\ \sigma_2 &= \sigma_{vM}\left(\eta + \frac{2}{3}cos[\frac{\pi}{6}(3 + \bar{\theta})]\right) \\ \sigma_3 &= \sigma_{vM}\left(\eta - \frac{2}{3}cos[\frac{\pi}{6}(1 + \bar{\theta})]\right) \end{aligned} \tag{2.10}$$

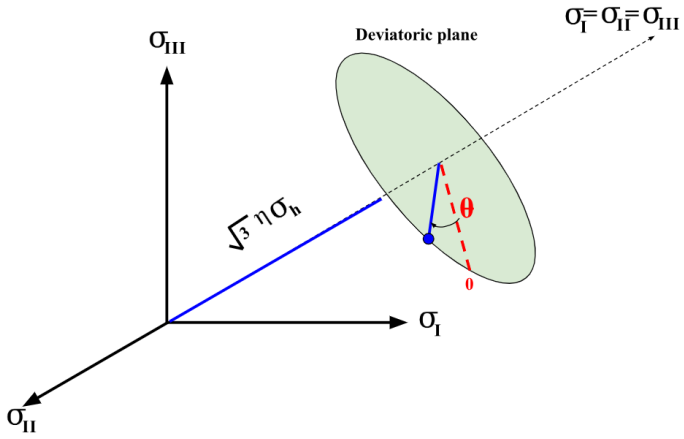

Figure 2.4: Haigh-Westergaard stress space, adapted from [26]

It can then be seen how von Mises equivalent fracture stress can be both represented with principal stresses and variables in the Haigh-Westergaard space: $\sigma_{f,vM} = \sigma_{f,vM}(\sigma_1, \sigma_2, \sigma_3) = \sigma_{f,vM}(\eta, \bar{\theta})$. Equivalently, one may represent the general fracture criterion for strain strain in these coordinates $\varepsilon_f = \varepsilon_f(\eta, \bar{\theta}$,MAT) where MAT is an arbitrary set of material parameters for this general model. This transformation reduces the four-dimensional fracture space ($\varepsilon_f = \varepsilon_f(\sigma_1, \sigma_2, \sigma_3)$) to a more intuitive three-dimensional one ($\varepsilon_f = \varepsilon_f(\eta, \bar{\theta})$) as shown in Figure 2.5. This is why failure models in this stress state space are referred to as 3D failure models. In Figure 2.5, 11 different curves are plotted for different Lode parameters giving a relationship between triaxiality and a corresponding failure strain found experimentally, and the technique is here to interpolate a failure strain for any Lode parameter or triaxiality. Of course the function $\varepsilon_f(\eta, \bar{\theta})$ is in reality a 2D surface but the interpolation between the curves handles this for the 11 curves.

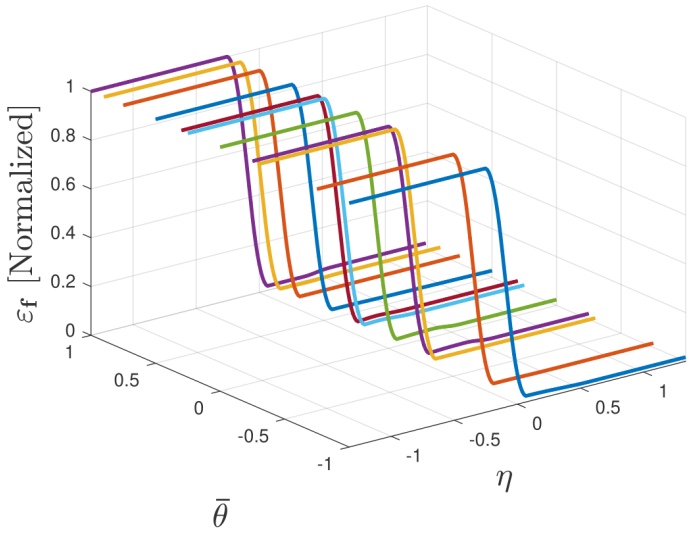

Figure 2.5: LS-Dyna MAT16351 failure curves in Heigh-Westergaard space (normalized)

2.4 Failure types

Far beyond the yield limit, large plastic deformation leads to nucleation, growth and coalescence of voids that cause material failure [10]. In the strictest sense of the word, *failure* refers to the point at which a material or component can no longer perform its intended function, often associated with excessive deformation, yielding, *instability* or fracture. *Fracture* itself on the other hand, denotes the loss of material continuity due to stress, typically manifested as the initiation and propagation of a crack. While related, failure and fracture are not the same. For this investigation there are two relevant and related schools of thought that are based on this idea of failure. One approach is to define failure criteria based on the stress state, i.e triaxiality and Lode. When these criteria are met, failure and fracture occurs. The other approach is to define a damage variable that is coupled with failure depending on the stress state, which again is in the Haigh-Westergaard space. This damage variable is intended to mimic the growth and coalescence of voids in the material. The first approach is how the failure model CrachFEM predicts failure and the second approach is what GISSMO is based on. Since CrachFEM has its roots in sheet metal forming, it is best suited for shell elements, while GISSMO is generally better for solid elements as shown in a previous thesis conducted for VCC [3].

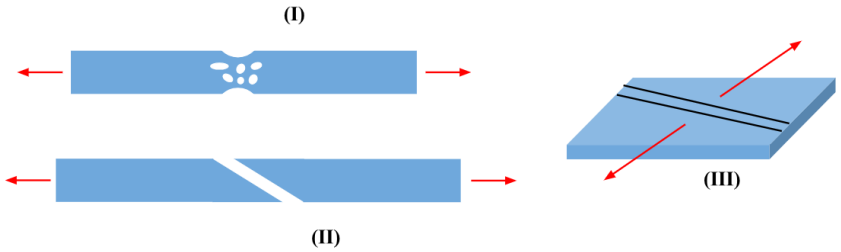

Figure 2.6: Failure types: Ductile normal fracture (I), Ductile shear fracture (II), Instability (III). Adapted from [25]

2.4.1 Ductile normal fracture

Ductile normal fracture as shown in Figure 2.6.I is the growth and coalescence of micro-voids/cavities that form a fibrous crack surface perpendicular to the load direction after significant plastic deformation. This physical observation is important for the qualitative analysis of the failure behavior of the physical tests.

CrachFEM characterizes the risk of ductile normal fracture as a failure criterion under the following models (since CrachFEM was developed for shells, plane stress is assumed thus new parameters for triaxiality have to be defined, and so suffix 'c' for 'CrachFEM' is added to avoid confusion):

$$\eta_c = \frac{\sigma_1 + \sigma_2}{\sqrt{\sigma_1^2 - \sigma_1\sigma_2 + \sigma_2^2}} = \frac{-3p}{\sigma_{vM}} \tag{2.11}$$

$$\beta = \frac{1 - MAT * \eta_c}{\sigma_1/\sigma_{vM}} = \frac{1 - MAT * \eta_c}{\frac{\eta_c}{3} + \frac{2}{3}cos[\frac{\pi}{6}(1 - \bar{\theta})]} \tag{2.12}$$

The equations used for failure strain are considered intellectual property, but it is known that the failure criteria is a function of η_c and β as well as material constants that are chosen to represented as 'MAT' [25].

$$\varepsilon_{pfn} = \varepsilon_{pfn}(\beta, MAT) = \varepsilon_{pfn}(\eta_c, \bar{\theta}, MAT) \tag{2.13}$$

2.4.2 Ductile shear fracture

Ductile shear fracture in Figure (2.6.II) is characterized by the formation of shear bands in the presence of shear loading conditions that lead to sliding along the plane of the crack. These shear bands are localized zones of plastic deformation and can also be seen in a sense as microcavities, but the crack that forms is much smoother than the fibrous normal fracture and almost looks like brittle fracture. CrachFEM defines a new variable θ_c to better capture the state of shear in the material (it has been given a suffix 'c' for CrachFEM to not to be mistaken for the Lode angle θ or LAP $\bar{\theta}$):

$$\theta_c = \frac{1 - MAT * \eta_c}{\tau_{max}/\sigma_{vM}} \tag{2.14}$$

$$\tau_{max} = \frac{\sigma_1 - \sigma_3}{2} = \frac{\sigma_{vM}}{3}(cos[\frac{\pi}{6}(1 - \bar{\theta})] - cos[\frac{\pi}{6}(3 + \bar{\theta})]) \tag{2.15}$$

Once again, the failure strain criteria for shear fracture defined by CrachFEM is intellectual property and so it is displayed here only to show its dependence on the stress-state and material constants represented as 'MAT'.

$$\varepsilon_{pfs} = \varepsilon_{pfs}(\theta_c, MAT) = \varepsilon_{pfs}(\eta_c, \bar{\theta}, MAT) \tag{2.16}$$

2.4.3 Localized necking

Localized necking is when deformation becomes concentrated in a small region under tensile stress leading to significant reduction in the cross-sectional area and this thinning can eventually lead to fracture. An important distinction is made here from *diffuse necking* which is also a reduction in cross-sectional area but occurs more gradually and is spread over a larger region in the material. Since it is such a local phenomena, one would need an extremely fine mesh in order to have the necessary resolution to simulate the behavior. Instead of doing this on account of computational expenses, the *risk* of localized necking is instead calculated and from here the failure strain from this type of instability can be approximated. Again this is intellectual property but this risk of localized necking is a function of triaxiality and LAP:

$$\varepsilon_{pfi} = \varepsilon_{pfi}(\eta_c, \bar{\theta}, MAT) \tag{2.17}$$

2.4.4 Failure coupling and Damage evolution

Material *damage* can be defined as the relative measure of properties between a damaged material and an undamaged material. On a microscopic level damage is usually seen as a void fraction in a representative volume. The incremental evolution of damage represents the nucleation, growth and coalescence of voids that are the cause of fracture [11]. On a macroscopic level this void fraction can be seen as the ratio between the total area A_0 and the effective resisting area A_{eff} after subtracting the microvoids and cracks from the reference area:

$$D = \frac{A_0 - A_{eff}}{A_0} \tag{2.18}$$

In this sense it can be said that (undamaged) $0 \leq D \leq 1$ (broken). The damage and true stress can then be coupled such that:

$$\sigma_{true} = \sigma_{eff}(1 - D) \tag{2.19}$$

Rather than to actually measure or model the effective area versus a reference area, it is instead prudent to relate this phenomena of damage to damage accumulation and evolution. Damage is often assumed to be connected to the plastic deformation history and so strain damage models often define damage as the ratio between current plastic strain and failure strain where for general models the ratio is not necessarily linear, hence the so called damage exponent n. The following derivations were taken from the LS-Dyna Developer Forum 2011 from DYNAmore, the company that developed GISSMO [26].

$$D = (\frac{\varepsilon_p}{\varepsilon_f})^n \tag{2.20}$$

The incremental damage is then defined by taking the derivative of 2.20 with respect to the plastic strain ε_p:

$$dD = \frac{n}{\varepsilon_f^n}\varepsilon_p^{(n-1)}d\varepsilon_p = \frac{n}{\varepsilon_f(\eta,\xi)}D^{\frac{n-1}{n}}d\varepsilon_p = g(\varepsilon_f, D, n)d\varepsilon_p \tag{2.21}$$

Under proportional loading, the damage increment can be integrated as:

$$D = \int_0^{\varepsilon_f} g(\varepsilon_f, D, n)d\varepsilon_p = 1 \tag{2.22}$$

In other words, failure is reached when $D = 1$ at $\varepsilon_p = \varepsilon_f$. It should be noted that just like with the other failure criteria, the damage is a function of the stress state defined by the triaxiality η and Lode parameter ξ.

In GISSMO the damage is also coupled to instability, more specifically *diffuse* necking. There are many models for instability, often the instability strain curve can be defined with the stress state η such that $\varepsilon_i = \varepsilon_i(\eta)$. A plastic instability variable F_i is defined as the non-linear ratio between the current plastic strain ε_p and the instability strain ε_i:

$$F_i = (\frac{\varepsilon_p}{\varepsilon_i})^n \tag{2.23}$$

Thus the incremental instability evolution becomes:

$$dF_i = \frac{n}{\epsilon_i(\eta)} F_i^{\frac{n-1}{n}} d\varepsilon_p = h(\varepsilon_i, F_i, n) d\varepsilon_p \tag{2.24}$$

$$F_i = \int_0^{e_i} h(\varepsilon_i, F_i, n) d\varepsilon_p \tag{2.25}$$

Note that for non-proportional loading, damage and instability criteria do not necessarily reach unity at ε_f and ε_i respectively:

$$D = \int_0 g(\varepsilon_f, D, n) d\varepsilon_p = 1 \tag{2.26}$$

$$F_i = \int_0 h(\varepsilon_i, F_i, n) d\varepsilon_p \tag{2.27}$$

The damage at $F_i = 1$ is defined as D_c, the critical damage at instability. At this point after $F_i = 1$ a coupling is then made between the stress and the current damage:

$$\sigma_{true} = \begin{cases} \sigma_{eff} & \text{if } F < 1 \implies \quad D \leq D_c \\ \sigma_{eff} \left(1 - \left(\frac{D - D_c}{1 - D_c}\right)^m\right) & \text{if } F = 1 \implies \quad D > D_c \end{cases} \tag{2.28}$$

Where m is a so called 'fading exponent'. When an element has a damage $D = 1$ it is said to have failed, and this is easily seen from 2.28 where it leads to $\sigma_{true} = 0$ and so this element is deleted. After instability is reached, the damage accumulated starts to impact the stress and the gradual decrease in stress can be seen as a form of element erosion or fading. The exponent m decides the rate of this phenomena, hence the name *fading exponent*.

2.5 CrachFEM

The way CrachFEM works is that it uses all the three failure criteria (Eq. 2.13, 2.16, 2.17) to form a strain failure surface and should an element in the simulation experience a plastic strain above the surface for a given stress state point $(\varepsilon, \eta_c, \bar{\theta})$, then that element has failed and will be deleted. CrachFEM is a failure model and will not decide the elastic or plastic hardening response of the material, however much work is still needed to calibrate so called *material cards* to ensure that failure occurs when it should. This calibration is done through a myriad of different tests to find values for the material parameters that have been represented as 'MAT'. In order to alter the material properties of a CrachFEM developed card, the hardening curves can be scaled to adjust the stiffness response (this is actually MFGenYld) and the strain failure criteria can be scaled to adjust ductility.

2.6 GISSMO

GISSMO is short for *General Incremental Stress State dependent damage MOdel* and relates failure to a damage parameter D, and couples damage with instability with parameter F_i as described in chapter 2.4.4. Since damage is a function of failure strain many tests are needed to calibrate *material cards* in order to find the failure strain $\varepsilon_f(\eta, \bar{\theta})$ which itself is a function of the stress states triaxiality and LAP. This data is what is represented in Figure 2.5. In GISSMO the cards also calibrate the damage exponent n in equation 2.21 as well as the fading exponent m in equation 2.28. During numerical calibration the cards are also calibrated for mesh regularization to reduce mesh refinement sensitivity.

2.7 Material cards

The material cards are one of the most central parts of this investigation as they determine the material response such as hardening curves, plasticity and failure criteria. These cards are calibrated from test data; a task that is expensive both in terms of time and money. All the used material cards rely on MFGenYld, developed by the company MATFEM, for the elastic and plastic response. The version of MFGenYld that is used is specifically calibrated for cast aluminum. Note that the naming of the cards is quite arbitrary and is simply taken from the names of the cards as given by VCC. In this investigation the following material models are used:

Table 2.1: Material Categorization

Failure Model	El. Type	Material Cards
CrachFEM	Shell	MAT16321, MAT16324
GISSMO	Tetra	MAT16351, MAT16564
GISSMO	Hexa	MAT16352, MAT16564

Note that MAT16351 and MAT16352 are outsourced solid cards from Dynamore and are calibrated the same way only they each are specifically made to be used with either tetra- or hexahedral element types. The solid card MAT16564 works for both tetra- and hexahedral elements and is an in-house scaled version of an outsourced card. Furthermore, as mentioned in chapter 2.8 some material cards can apply scatter or be deterministic, and it should be noted 16564 is stochastic (applied scatter) meaning it will apply scaling to hardening curves and failure strains to random elements. This is meant to imitate the random distribution of imperfections in the cast material.

Returning to the hardening curves in Figure 2.2, the CrachFEM material cards *MAT16321* and *MAT16324* have been calibrated with Modified Ghosh 2.2 while the GISSMO card *MAT16564* as well as the GISSMO card calibrated by Coric and Seyedraoufi in their 2024 thesis [1] was calibrated for Hocket-Sherby hardening 2.1. The GISSMO card *MAT16351* has tabulated data without revealing precisely which hardening model(s) were used. The strain failure curves for the CrachFEM cards are

all described by the failure criteria (Eq. 2.13, 2.16 & 2.17) and for GISSMO cards failure is governed by damage evolution and the strain failure curves in Figure 2.5. In other words hardening and strain failure are governed by curves and these curves can be scaled to alter the simulated materials characteristics. From these curves it is possible to directly make a material more or less ductile and have a higher or lower tensile strength, which is interesting when one wants to account for process related imperfections in the material.

2.8 Cast Aluminium: Process mapping and common imperfections

As mentioned, the megacast part as well as the snake-tool detail are cast using a process called High Pressure Die Casting (HPDC). In order to further understand and explain fracture phenomena, some knowledge of this production process is required, especially since this study includes process mapping and qualitative observations of the fracture surface. The physical process behind HPDC is using molten metal, in this case aluminium, and forcing it into a shape cast die at high speed and pressure. Upon solidification the die is released and the detail is ejected. For this investigation, simulations of this process have been done in the CAE software *ProCast* and to study process parameters there are three main nodal values that are exported: flow length, solidification time and shrinkage porosity. In this case, the latter two are of most interest since the beam itself has roughly a constant flow length due to the flow direction being perpendicular to the beam length. The reason for studying these is because they are directly related to casting imperfections. It should be noted that the theory behind how casting modeling works is extremely sophisticated and is an endeavour that has attempted to be perfected for the last 40 years or so. However, there is still work needed to be done regarding accurately capturing the appearance and nature of imperfections in the material [18]. Instead of trying to predict imperfections with simulations, it is also possible to directly observe imperfections using a 'Computed Tomography Scan' (CT-scan) of the cast part. From such a scan it is also possible to export numerical data defining the level of imperfections. The benefit of using simulated process data is that it is a powerful tool for predicting levels of porosity without having to actually cast the part. The drawback is that it is only a simulation and not the observed truth which the CT-scan is. The drawback of the CT-scan is that there is a limit on the size of the part that can be scanned, the scanning resolution and that the part has to be successfully cast first making it much more time consuming and cumbersome to acquire this data.

There are many types of imperfections that can arise during casting processes such as metallic projections, swells, cavities, discontinuities, imperfect surfaces, incomplete casting, incorrect dimensions, inclusions, etc, all of which influence the mechanical properties of the cast part. Most relevant to this investigation are the formation of cavities which can be classified as blowholes, pinholes and shrinkage cavities. Blowholes are larger cavities caused by trapped air or gas while pinholes are smaller holes on the surface due to trapped gases. Shrinkage cavities are voids formed due to the

contraction of the molten metal as it cools, often a symptom of insufficient metal supply or low pressure [13]. This can happen on a macroscopic or a microscopic level where dendrites that form and coalesce as the metal cools form empty voids in the material. Porosity has been observed to significantly reduce ductility and increase scatter in material properties according to studies [20], and was investigated by Coric and Seyedraoufi at VCC in 2024 [1]. It should be noted that the exact same alloy that they studied in 2024 is being used in this investigation. They found, for example, that a maximum pore size of only $2.2 \times 10^{-3} mm^3$ in a standard tensile test coupon gave a >25% decrease in failure strain. Studies by Cáceres [21] characterized porosity by cross section surface void fraction and found that 1% porosity resulted in 10% reduction in tensile strength and a 90% reduction in elongation to failure. Thin details are therefore particularly vulnerable since all pores become relatively more significant when considering the cross section. The scattering together with the influence on ductility mean that both failure strain and damage initiation are expected to stochastically vary which intuitively makes sense since no detail can be cast exactly the same way twice due in large part to turbulence. This is also why some models include stochastics to get the full range of possible outcomes due to scatter.

Process data mapping is taking material 'characteristics' that arise from casting, such as porosity, and relating those onto a corresponding CAE model that can subsequently be simulated for different load cases. The idea is to accurately capture the behavior of the porous material by mapping the location and magnitude of the imperfections onto the CAE model. This has been accomplished for cast aluminium by taking material characteristics from process simulation data [4], but it is shown in this investigation that it can also be done for CT scans, although it has not been done before at VCC.

2.9 Isogeometric Analysis

The theory behind isogeometric analysis (IGA) is only described briefly.
IGA was developed with the goal of enabling CAD engineers and CAE engineers to work on the same geometry. Modern CAD relies on non-uniform rational B-splines (NURBS) to discretize components, which therefore becomes the natural choice for the IGA isoparametric formulation. This means the CAD geometry can be matched exactly with the FEA, increasing precision in for example contact problems [22].

Dyna do however mention two main drawbacks limiting practical implementation. Firstly the behavior of solid elements is not yet fully understood. Second, the CAD geometry may need to be cleaned and modified, since geometries often are built from a collection of surfaces [22]. Implementation will be discussed further in the methodology chapter.

3

Methodology

The following chapter presents the methodology used to obtain the results, divided into two main sections: physical testing and simulations. The simulation section covers general FEM modeling, mapping, and IGA. Both the physical and simulated tests focus on a three-point bending test. It was observed that the simulations over-predict the strength of the beams, leading to an investigation into the causes of this overestimation and how to incorporate imperfections into the model for greater accuracy.

3.1 Physical testing

The following section outlines the testing procedure, both how specimens were prepared, how the testing itself was conducted, and the post-processing of the results. The purpose of the testing is most closely related to the first two objectives of the investigation, namely to carry out physical testing to understand the material response on a *component* level, but also to investigate the extent that recycled material impacts the material response. The physical testing also serves as a point of reference for the simulations. The main quantitative metrics that are evaluated are maximum force, displacement at failure and energy absorption.

3.1.1 Preparation of test samples

The physical testing was conducted on beams extracted from castings of '*SnakeTool 1.5*'. The casting of the beams was outsourced. In preparation for the testing, the beams were first separated from the snake tool using a band saw. The position in the snake tool from which the beams were extracted is shown in Figure 3.1. The cut surfaces became rough and uneven and a choice was made to mill them to ensure uniformity and a more even surface. A flange on the beams short end was also removed.

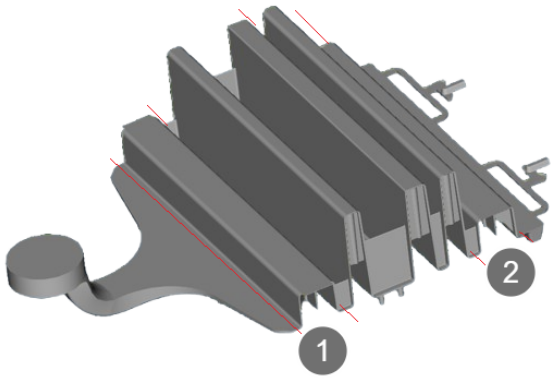

Figure 3.1: Snaketool 1.5 with Beam extraction positions, inlet is shown to the left

Additionally the beams were also paint-baked. Paint-baking is a process where the component goes through the same heat treatment that would be involved when parts are painted. This process can alter the mechanical properties of the part slightly. It is therefore desirable to subject the test specimens to this to more closely match the material characteristics of the material in the component.

The beams and the quantity of each alloy obtained from the manufacturer are presented in Table 3.1. The primary alloy is aluminium as bought from the supplier while the secondary alloy is recycled material but tested to ensure that it has the exact same chemical composition as the primary alloy. The secondary alloys 'B2' and 'B3' contain increased levels of iron and vanadium intended to represent a recycled material. This range of batches will give an indication of the reliability of recycled material in accordance with the second point of the objectives.

Table 3.1: Test specimen inventory

Snaketool position	Alloy	Alloy abbrev.	No.
B1	Primary alloy	A4	4
B1	Secondary alloy	B1	3
B1	Secondary alloy, increased Fe	B2	2
B1	Secondary alloy, increased Fe, V	B3	1
B1	"Scrap" beams	W5	3
B1	Primary alloy, no paint-bake	A4*	1

Please note that no beams are from the second position in the snake tool, which limits the ability to test the influence of flow length, since the flow length variation within a single beam is not enough to investigate this property. To minimize waste of high-quality specimens during setup, "scrap" beams are used for initial testing of the rigs. Note also that the names of the beams describe the beams: which alloy they are, which number they were in the production sequence and which position in the snake tool they come from. For example a beam named *A4-109-B2* would be of primary alloy, was 109th in casting sequence, and comes from position *B2* in the snake tool. In some occasions the last *B1* has been omitted in the nomenclature

since all beams come from the *B1* position. In total, 11 three point bend tests were conducted[1].

For collecting the data, a force transducer was synced to an ARAMIS Digital Image Correlation (DIC) system using Dewesoft. With DIC it is possible to track the displacement of the impactor, and when synced to the force transducer the force-displacement curves can be obtained. The DIC system was also used for measuring the displacement field of the center section of the beams. To utilize the DIC, the beams needed to be painted due to the lack of a natural, recognizable pattern. First, the beams are painted white, then lightly sprayed with black to create a heterogeneous dotted pattern. The side that was expected to fail first is painted and monitored with the DIC equipment whereby the relative movement of the painted dots give information about the displacement field on the surface of the beam. Three additional cameras were set up to capture the underside with the purpose of understanding the failure mode for each beam. From initial simulations it could be seen that the beam occasionally broke first in the middle of the webbing. It was therefore interesting to monitor where the fracture was initiated, and the underside was hard to capture with the DIC.

3.1.2 Physical testing

As stated in the first objective, the test performed was a three-point-bending.

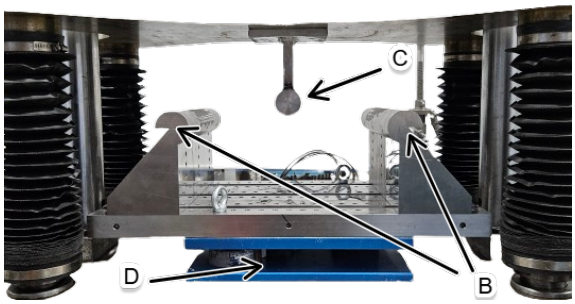

Figure 3.2: Three-point-bend test rig

The three point bending test was set up according to Figure 3.2 with a c-c distance of $400mm$ between the supports. The supports are semicylinders with a diameter of $60mm$ and the impactor a diameter of $50mm$. The entire test setup had already been manufactured and it was merely a process of changing the distance of the supports and mounting it in the Universal testing machine (Tinius-Olsen, hydraulic compressor). The impactor (C in Figure 3.2) was placed equidistantly from the two supports (B in Figure 3.2). The entire support rig was placed on a force monitor (D in Figure 3.2) for the ARAMIS DIC system which was used to get the force-displacement curve. The setup is assumed to be level, and great efforts have been made to make sure the impactor is parallel to and placed in the middle of the supports. Much care was also taken to make sure the beam was placed orthogonally to the impactor and

[1]Note that some beams were sawed in half, with the intention of doing axial crush tests. This was abandoned due to a lack of time

the supports. The measurements were made using tape measure, square ruler and a digital angle finder. While more accurate than visual estimations, it still introduces some inaccuracies. The ARAMIS DIC cameras were angled roughly 45 degrees and pointed from above the beam so that the displacement field of the flange could be captured.

3.1.3 Qualitative analysis

A qualitative analysis was also carried out for two main purposes. The first being as a means of further validating the CAE model to ensure that the beam is fracturing in the same way as the physical results. For this cameras were set up as seen in Figure 3.3 whereby camera A filmed from below, camera C captured the front of the beam and an identical camera C is placed in the back. Camera B is the ARAMIS DIC camera that captures the strain field. The second purpose of the qualitative analysis is to better understand the potential casting imperfections and this was later used for mapping as discussed in chapter 3.3. To accomplish this, fracture surfaces from 5 beams (Table 3.2) were photographed using stereo-microscopes. The beams were chosen based on which beams that were the strongest and weakest out of primary batch material as well as in total. A B3 beam was also analyzed since it is of interest to see its level of porosity given that it is the least chemically pure alloy.

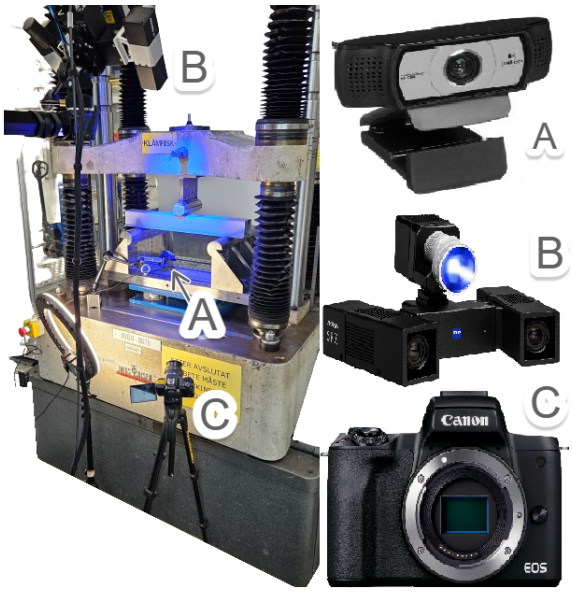

Figure 3.3: Camera set-up for qualitative comparison

Table 3.2: List of fractography beams

Beam	Note
A4-111-B1	Best primary beam
A4-112-B1	Worst primary beam
B1-135-B1	Best beam
B2-150-B1	Worst beam
B3-176-B1	To cover all batches (A4, B1, B2, B3)

CT-scanning was also used as a method of collecting qualitative data. The CT-scan was conducted at the VCC material lab. The scanning had to be divided in two and then pasted together since the beam was too big to fit in one. The beam that was CT-scanned was beam A4*-102-B1. The goal with the CT-scan was to gain qualitative data to assess the porosity in the part, as well as to gain quantifiable data as a basis for the CT-scan based mapping. A refined scanning was also done where the voxel-size was reduced to capture even smaller pores.

The beam that was CT-scanned was not part of the initial testing sequence, making it necessary to ensure its load-bearing capacity and failure behavior are representative. Notably, this beam has not been paint-baked, and testing it separately from the main batch increases the risk of differing circumstances, potentially leading to misleading results. A comparison of force-displacement results between main batch tests results and *A4*-102-B1* can be found in appendix B.

3.2 Finite Element Modeling

This chapter describes the FEM modeling, including specifications of the solution parameters used, how the test rig was modeled and what kind of boundary conditions that were applied. It also describes the first steps to making the model more accurate, as well as investigations into how the results are impacted by use of different types of element types and formulations. In general, each improvement in the analysis workflow builds upon the previous steps. The process began with a mesh sensitivity study, which identified the mesh that provided the best balance between accuracy and computational cost. This mesh was then used in the subsequent geometry evaluation. Following that, both the element study and the mapping were performed using the geometry and mesh that, at that point, were considered to be of the highest quality.

3.2.1 Meshing routines

To investigate the difference between shell and solid element formulations, both a solid and a shell mesh are required. At VCC, the mesh size used in complete vehicle simulation is a target length of 3.4 mm. This is also the reason for the mesh study starting at 3.4 mm rather than 3.5 mm. Despite the increased computational cost, the influence of finer meshes was studied. For this mesh size sensitivity analysis, one solid material model (MAT16351) and one shell material model (MAT16321) were

used and it was assumed that the other material cards would converge in a similar fashion. The mesh size was controlled by specifying both the target length and the minimum length of the elements. When discussing mesh size, the target length is primarily referenced. The mesh sizes used were $3.4, 3.0, 2.5, 2.0, 1.5, 1.0$ and 0.5 mm. Note that the same target length was used for both solid and shell elements, resulting in vastly different numbers of elements. For reference, meshing with a target length of 3.4 mm yields approximately $500,000$ solid elements and only $11,500$ shells elements.

To construct the shell mesh, a mid-surface was extracted. The geometry was simplified as solid intersections were reduced to connections of 2D surfaces. This mid-surface was then meshed with shell elements. The 3.4 mm shell mesh can be seen in Figure 3.4, along with the non-meshed part for reference.

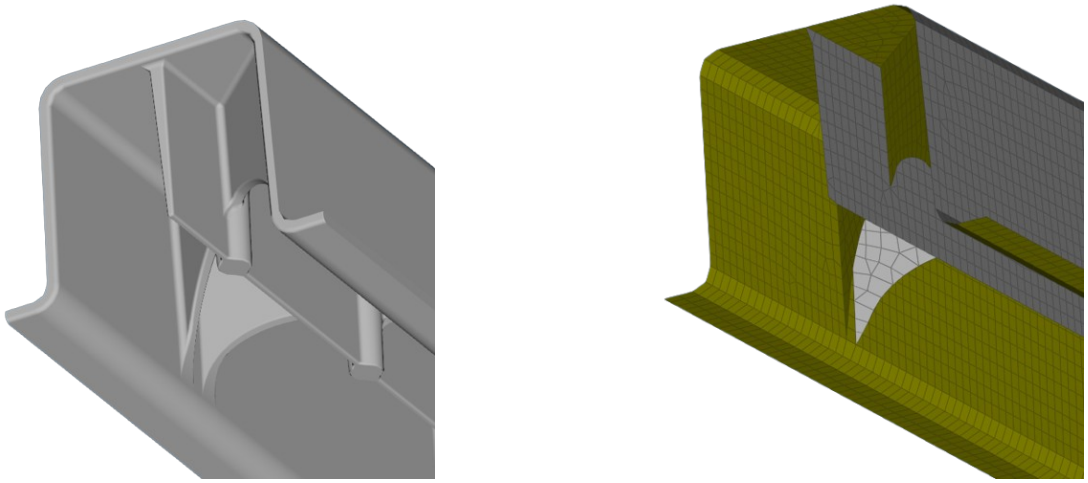

(a) Non-meshed reference part **(b)** Shell mesh

Figure 3.4: Comparison between meshed and non-meshed part

Finally, a comparison between tetrahedral and hexahedral solid elements was carried out in order to determine whether the time investment needed to create the hexahedral mesh is worth the potential benefits in accuracy and simulation speed. In general, hexahedral meshes are rarely automated as they are for tetrahedral meshes and for this investigation, symmetry of the beam was utilized to speed up the meshing process since the beam is effectively divided into 8 units of Figure 3.6. This was then stitched together carefully to preserve the geometry as much as possible. Theoretically a hexahedral mesh should not need much refinement if it captures the geometry accurately and to confirm this claim the hexa-mesh was refined with a built in function. In ANSA there is also a built in function called *tetra2hexa* that splits a single tetra element into 4 hexahedral elements, visualized in 3.5. In this investigation a tetra-mesh with a target length of 3.4mm was converted to a hexa-mesh (hence it was refered to as *3.4TETRA2HEXA*). This does however lead to elements with very poor aspect ratios (the ratio of element edge lengths) that can be a problem for accuracy. The three resulting hexahedral element beams can

be seen in Figure 3.7.

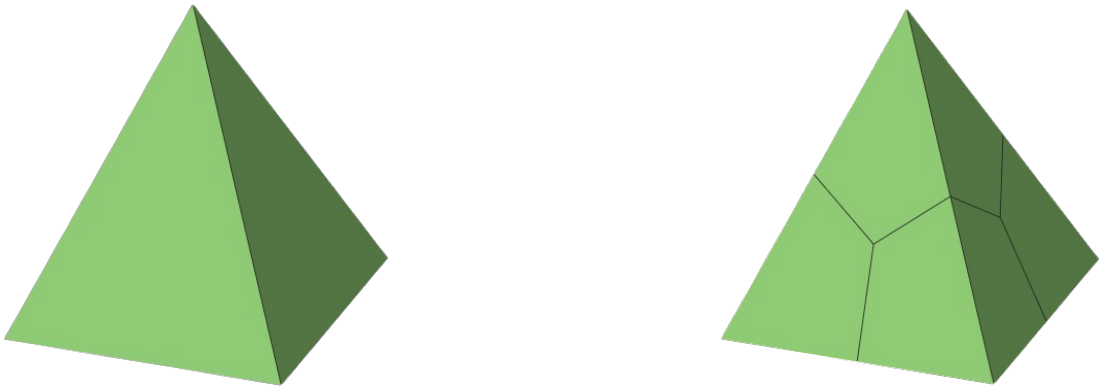

(a) Tetra element **(b)** Hex element

Figure 3.5: Visualization of conversion from tetra to hex elements

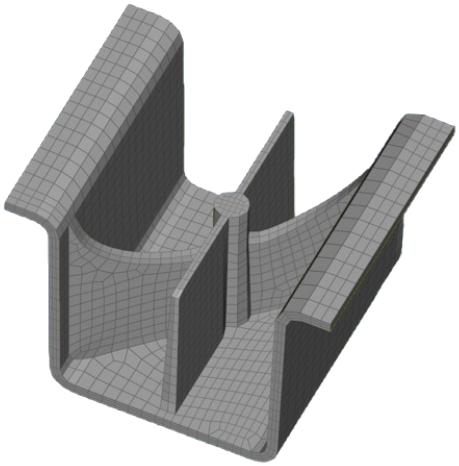

Figure 3.6: Symmetry utilization for hexahedral mesh assembly

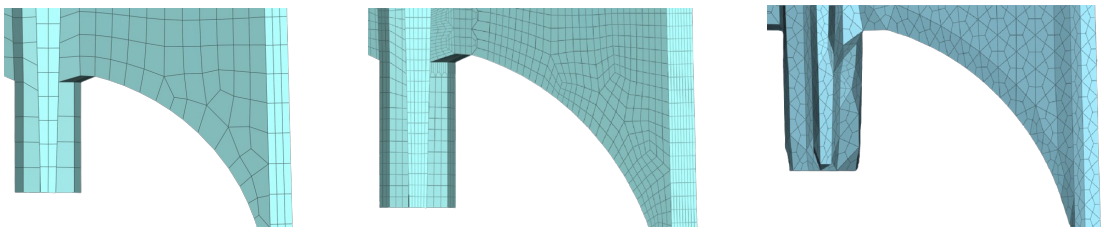

(a) Hexa **(b)** Refined Hexa **(c)** Tetra to hexa

Figure 3.7: Variations in the hexahedral meshing routine

The impactor was meshed with shell elements and the supports are modeled with solid elements. The reason behind having to mesh the supports and impactor is mainly that the mesh is used in the contact algorithm.

3.2.2 Boundary conditions and simulation parameters

The impactor is constrained in x- and y-directions, the displacement is prescribed in z-direction and the impactor is assumed to be rigid. The load curve of the impactor was defined as linear displacement from 0 to 80 mm in 100 ms and since the failure phenomena is assumed to be strain rate independent, this load curve can be entirely arbitrarily chosen, as long as the displacement is large enough to break the beam and slow enough not to introduce dynamic effects. The beam is free to move and rotate in all directions and will deform and fracture in accordance with its material card. The supports are completely constrained and rigid.

For contact a penalty method was used, with friction coefficient of 0.15 (both static and dynamic) and a penalty scaling factor of 1. For simulations explicit time integration with a time step of 0.54 ms with a time scaling factor of 0.9 is used, and mass scaling is enabled if necessary. The friction coefficient was found by VCC while the simulation parameters were chosen to ensure stability at a reasonable run-time.

3.2.3 CAE Geometry Modification

For this study, a mesh with a target length of 2 mm was used for the solid meshes. For the shell elements, a target length of 1.5 mm was chosen.

During the experiments, it was observed that the beams deviated from the ideal *.stp* model. Measurements taken manually from the beams as well as the CT-scan was used to quantify the discrepancies between the cast geometry and the CAD model. To address this difference in the geometry, the CAE model was adjusted to better represent reality. The modifications included:

1. Cutting the flanges based on manual measurements from the test specimens.
2. Replicating the bow of the beam.
3. Manually reducing the thickness of the flanges and roof.

The flanges were cut to match the narrower dimensions observed in the actual specimens compared to the CAD model. The thickness was also adjusted, though these measurements were taken from the 3D scan. Two different approaches were taken, either the average or the minimum of a number of thickness measurements was used as the thickness of the entire region. The thickness reduction is presented in Table 3.3.

Table 3.3: Flange and Roof Thickness Reduction

Method	flange thickness	roof thickness
Original	3 mm	3 mm
Minimum	2.67 mm	2.59 mm
Average	2.73 mm	2.69 mm

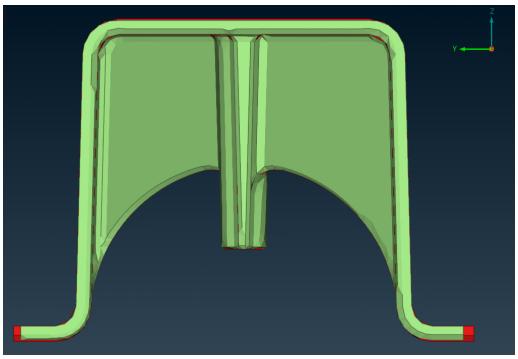

Figure 3.8: Cutting modification done to the flanges and thinning of the flange and roof

The 3D scan also indicated a slight bend in the beam, as shown in Figure 3.9. The middle points of the beam were approximately 0.9 mm lower than the outer points. To replicate this, a simulation was run to achieve the same bend as the 3D scan, and this modified geometry was used as the input for a new simulation. This process was applied to both shells and solids, representing the final type of geometry improvement.

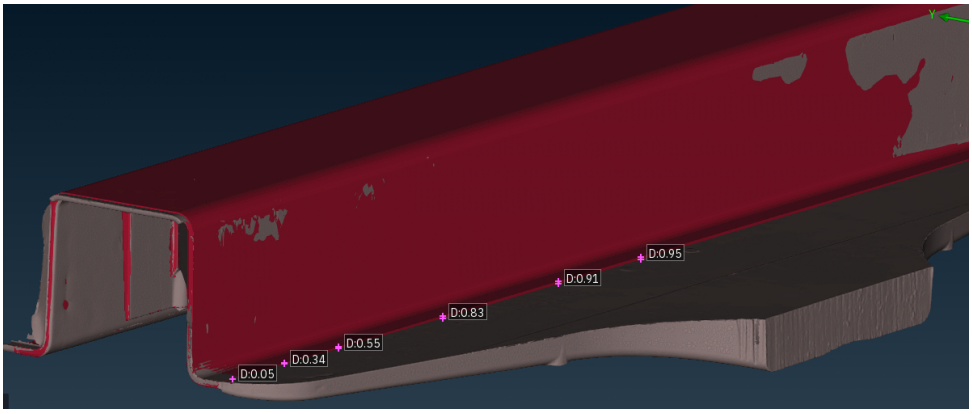

Figure 3.9: Comparison between CAD-geometry and 3D-scan (inlet is seen to the right)

Note also that the geometrical changes were made in succession, meaning the beam with reduced thickness also has cut flanges. This does not apply to the bow, see 3.10.

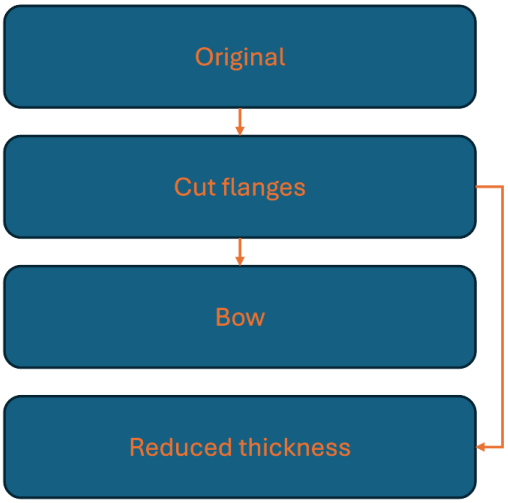

Figure 3.10: Geometry evolution schematic

3.3 Mapping

As previous studies concluded, porosity severely impacts both the strength and ductility. The physical testing also showed signs of the CAE models being too stiff and ductile. A hypothesis formed that accounting for porosity in the CAE models would increase accuracy, thus mapping took a much larger role in the investigation than initially intended. The project attempted to modify the FEA-model material parameters using two methods: Process Simulation Data based Mapping (PSDM) and CT-scan based Mapping (CTM).

There are two main underlying arguments for attempting the mapping, besides the discrepancy in the simulations versus testing. Firstly, porosity can be mapped to shell elements but pores themselves cannot be directly meshed with these element types. Second, some investigations into PSDM has already been done, so the pipeline has already been set up. The CTM mapping will as much as possible utilize this pipeline. In practice, mapping can be done on four different levels ranked from least to most intricate.

1. No consideration of porosity
2. Macro scaling
3. Micro scaling
4. Pore meshing

In this categorization, Macro scaling is composed of two techniques, *homogeneous scaling* and *Poor Man's Mapping*. Micro scaling is divided into CTM and PSDM. Micro scaling means changing the material properties on an element level using correction factors from RVE pore simulations inspired by Coric and Seyedraoufi [1].

Finally, pore meshing refers to the technique of geometrically meshing pores from CT-scan and inserting them into the CAE model while trying to balance computational expense and accuracy by treating the pores before they are inserted. These different levels are very much tied together and were all conducted in an endeavor to better match the results of the physical testing data. For example the scatter material model MAT16564, the homogeneous scaling as well as the Poor man's mapping serve as justifications that the material properties need to be scaled in some way. This data can be mapped and scaled on an element level.

PSDM uses data from casting simulations of '*SnakeTool 1.5*' in *Procast*. CTM is based on a scan that was performed on a representative beam, namely *A4-102-B1*. Since this particular beam was cast earlier than any beam tested previously (102 in the sequence, as opposed to the earliest previously tested number 110), it is not guaranteed to be representative of the rest of the beams. Additionally, *A4-102-B1* was neither paint-baked nor were the flanges cut, which further emphasizes the need to confirm representativeness. To make representativeness certain, a three point bend test was performed succeeding the CT-scan, see Appendix B.

3.3.1 Macroscaling: Homogeneous Scaling and Poor man's Porosity mapping

Both PSDM and CTM are highly complex and time-consuming processes. While there is existing infrastructure for mapping from process parameters, mapping from CT scans has not been previously undertaken. Therefore, while some foundational work on mapping was already established, it was prudent to confirm two things. First that a crude scaling of the material card could lead to less discrepancy between the simulations and physical results, and secondly that it could be accounted for with porosity. Upon confirming these, it would justify applying scaling to areas with high levels of porosity using CTM and PSDM. To address this, a homogeneous scaling was applied to the hardening curves and failure strains and an initial "poor man's porosity mapping" (PMM) was conducted by reducing the center rib. The scaling of hardening curves and failure strain would intend to reduce the strength and ductility of the models. The main evidence supporting the deletion of elements is the results from examining of the fracture surfaces and CT scanning, as well as the video footage of the physical tests paired with the force-displacement graphs.

The new solid tetra and shell geometries are shown in figures 3.11a and 3.11b.

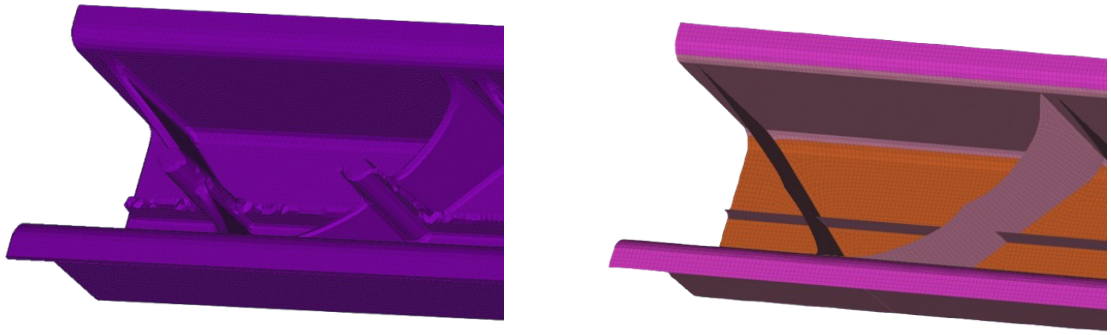

(a) Tetra-meshed beam with reduced central rib

(b) Shell-meshed beam with reduced central rib

Figure 3.11: Comparison of PMM FEM geometries

3.3.2 Porosity meshing

As a straight-forward method of including the porosity in the FEA model, the pores found from the CT-scan were directly meshed into the beam. First the pores are isolated and meshed from the CT-scan and the beam geometry is given a triangular element surface mesh. After this the beam and the pores are aligned and finally a solid meshing of the beam is carried out which leads to cavities being formed around the pores. The pore mesh can then be removed and the shell mesh of the beam released and deleted, then one is left with a solid beam with pore cavities as seen in Figure 3.13. In order to have a reasonable number of elements, the pores need to be made more coarse as seen in Figure 3.12, and in this investigation each pore is wrapped and remeshed with a target length of 0.5 mm. This has drawbacks that are discussed in later chapters.

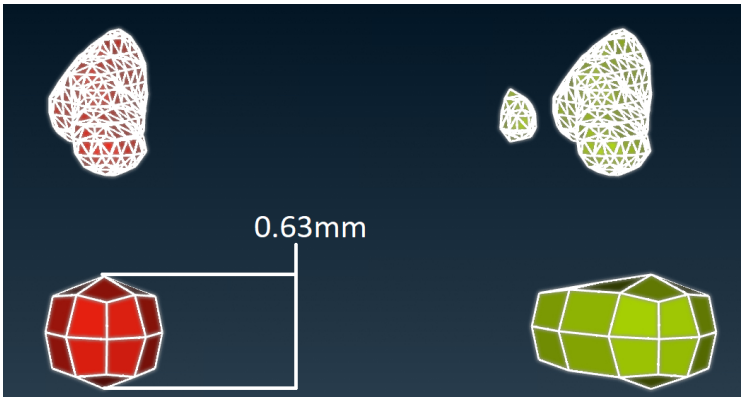

Figure 3.12: Pore wrapping

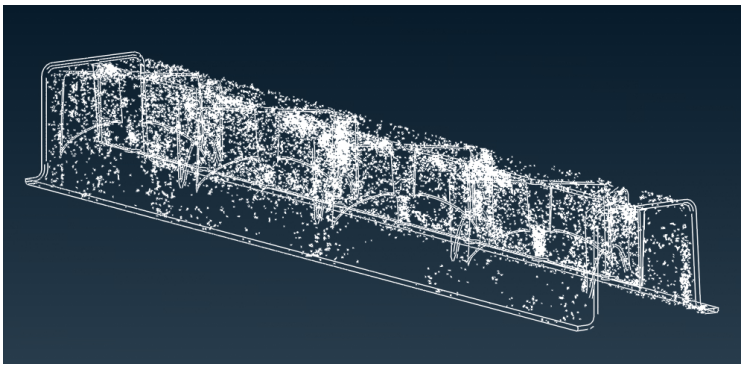

Figure 3.13: Insertion of pores into solid mesh

3.3.3 Failure strain and hardening scaling

For this scaling based on level of porosity, RVEs were constructed and exposed to loading until failure. Reaction force curves were then used to produce stress-strain relationships varying with pore size serving as a basis for the scaling of material properties. The RVEs were 1 mm^3 cubes that were meshed finely into which an artificial pore is inserted. It aims to answer the question "If an element of volume 1 mm^3 had a pore fraction of f, how would one need to scale it's material properties in order for it to respond the same way without meshing an actual pore?". For simplicity the pores in the RVEs are perfectly spherical and centered in the cube as shown in Figure 3.14. Note that this is a simplification, since Coric and Seyedraoufi showed that pore geometry, location and clustering also play a role in material properties [1]. In this investigation these effects are ignored since the mapping techniques are not sophisticated enough. The bottom set of nodes are constrained from moving out of the plane, and to constrain rigid body movement a corner node is constrained from movement. The top nodes are prescribed with a displacement in the vertical direction, but are free to move in the plane.

The process of scaling based on volume fraction and using RVEs is as follows:

1. Nine different levels of porosity volume fractions (0%, 1%, 5%, 10%, 15%, 20%, 30%, 40%, and 50%) are converted to spherical pores of a certain radius.

2. A pore of corresponding radius is inserted into the $1 \times 1 \times 1$ mm block and is meshed.

3. The RVE is subjected to loading and a stress-strain curve is measured from the simulation.

4. A RVE with no pore is simulated but with scaled material properties to match the behavior of the RVE with a meshed pore.

The hardening curves that are to be scaled are the ones seen in Figure 2.2 while failure strains are related to Lode and triaxiality which are controlled by the curves seen in Figure 2.5. Scaling factors for hardening curves are taken as the ratio of the stress at onset plastic hardening for an RVE with no void and an RVE with a given

void as seen in equation 3.1. The same approach is then made for scaling failure strain $\varepsilon_f(f_i)$ as in equation 3.2.

$$s_h(f_i) = \frac{\sigma_Y(f_i)}{\sigma_Y(f_0)} \tag{3.1}$$

$$s_s(f_i) = \frac{\varepsilon_f(f_i)}{\varepsilon_f(f_0)} \tag{3.2}$$

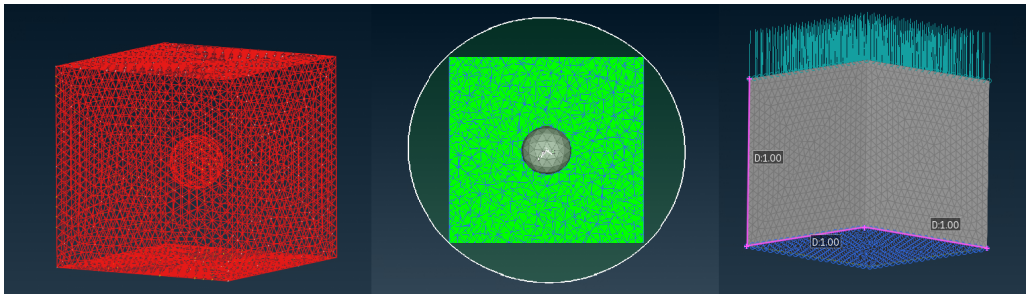

Figure 3.14: Representative volume element, 1% porosity: a) Pore insertion, b) RVE cross section, c) Boundary conditions

3.3.4 Mapping of process simulation data (PSDM)

Two geometrically identical meshes are needed for the mapping, a process simulation mesh containing porosity data stored in the integration point of every element, and a "receiver" mesh. The receiver mesh is in this case is the FEA-mesh.

Around the nodes of the casting simulation mesh, hexahedral elements are created and given history variables that correspond to the casting data creating a so called hex-cloud. This is now the 'donor' mesh which is then mapped to the receiver mesh. Mapping is done with radial basis function interpolation (RBF) and the output from this mapping is that each element in the receiver mesh now has a value for the casting simulation parameters such as porosity. Using these variables, one can scale for example hardening curves and failure surface. A hexcloud fringe plot is showcased in Figure 3.15a while a cross-section fringe plot of the porosity that has been mapped to the FEA-mesh is plotted in Figure 3.15b.

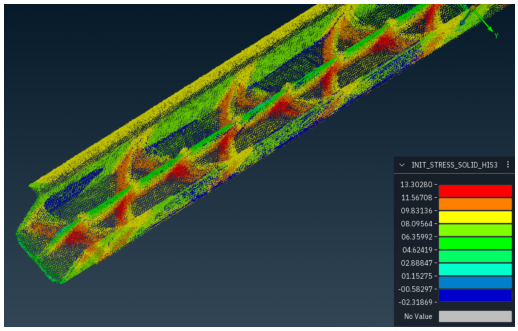

(a) Hexa-cloud, solidification time fringe plot only for illustrative purposes

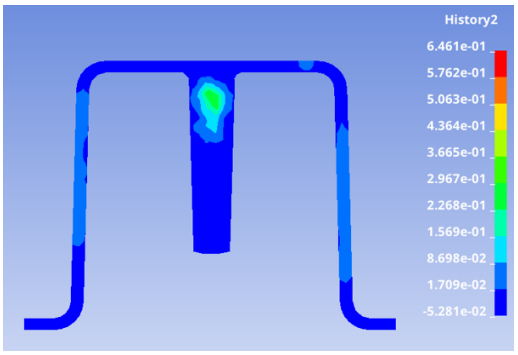

(b) Shrinkage Porosity fringe plot

Figure 3.15: PSDM data

3.3.5 CT-scan based mapping (CTM)

CTM is an approach that mirrors the procedure of the PSDM. A point cloud was extracted from the scanning software, which is used as the donor mesh where each point is associated with a value of void fraction. In other words if a volume $V = a_x \times a_y \times a_z$ contains a pore with volume V_p which is found simply via the CT-scan's grayscale and threshold value, then the void fraction is $f = \frac{V_p}{V}$. A grid of $a_x \times a_y \times a_z$ cubes was defined where each center point is given the value of f. These are then mapped to the receiver mesh using the built in function *RESULTS_MAPPER* so that the Gauss points of each element can be assigned the volume fraction.

3.4 Isogeometric analysis

As a proof of concept, we aim to investigate the feasibility of using isogeometric analysis (IGA) as an alternative to the traditional finite element method (FEM). IGA offers the potential for reduced computational costs and simplifies the preprocessing steps involved in simulation setup.
LS-DYNA has developed a temporary workflow for the use of IGA within their software. This involves loading a FEM mesh and applying an IGA keyword, enabling the solver to process the geometry and perform the analysis. The FEM mesh serves multiple purposes: it helps the solver understand the geometry, it is utilized in the contact algorithm, and displays results during post-processing.
For the practical implementation of IGA, two different mesh types are considered: the geometry and the background mesh. The workflow in LS-DYNA for IGA implementation is as follows, starting from an already functioning *.key run-file with necessary boundary conditions, material models etc.:

- Make a FEM solid tetra mesh for the part which is to be analyzed and export it as *tetra.k*

- In the `*box_template.k` file, specify:
  1. Material ID
  2. FE solid Part ID
  3. Box corner points
  4. Element edge length
  5. Integration rule
  6. Stabilization
- Include the *tetra.k* and **box_template.k* files in the run-file and run

Given the use of two meshes, the refinement study will take into account the sensitivity of both. For both studies the MAT16351 material model was used. It is worth noting that the IGA simulations only run on 24 CPUs, even though the *-NCpuauto* flag is set to 120. In relation, the FEM simulations are run on 120 or more CPUs, 128 in the 2 mm tetra case specifically.
In the implementation, two different meshes were utilized. For the background mesh, a homogeneous box-mesh was created, defined by the element edge length (EEL). This measurement specifies the side length of the elements in each direction, which, for this study, is uniform in all directions.

3.4.1 Geometry mesh study

The geometry study was done by taking the geometry from the new baseline and meshing it with tetras of a target length of the specified mesh size. The material was applied and the part was then extracted as *tetra.k* to fit into the IGA-template. The EEL for the geometry study was 2 mm.

3.4.2 Background mesh study

The mesh size of the Background mesh was varied by supplying different values of the EEL. The given EEL was one and the same for all directions. Note that the geometry used in this study has a mesh target length of 2 mm and the material was MAT16351.

3.5 Tensile test material validation

As a final validation point, the material cards were compared to tensile tests that were performed on the same casting component (snaketool 1.5) for the different batches A4, B1, B2 and B3. This physical data was collected by a parallel thesis investigation at VCC more focused around developing the material cards themselves than CAE modelling [19]. The intent of this comparison was to determine first how well the cards performed in this much simpler testing case and secondly to establish whether there was statistically significant difference between batch data on a simpler level. This is once again in order to fulfill the second objective of

this investigation which is to examine the extent that recycled and increased levels of iron and vanadium impacts the material response. The coupon dimensions are found below in Figure 3.16.

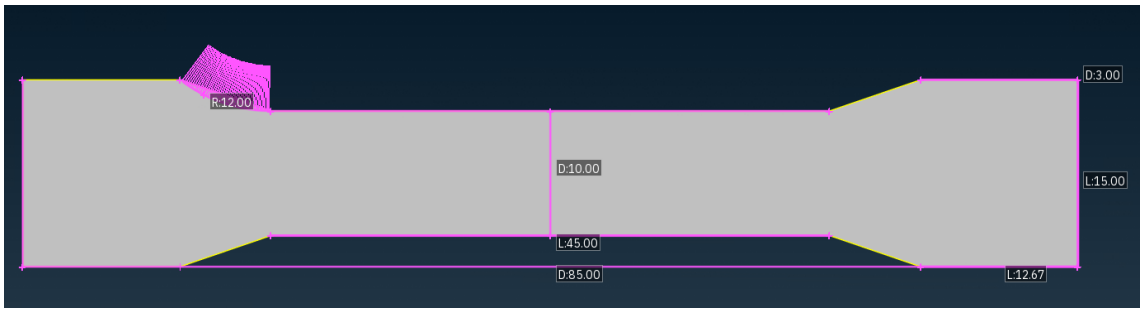

Figure 3.16: Coupon for tensile tests

4

Results and discussion

This chapter presents the results, structured in two main sections: physical testing and simulations. The physical testing section includes both qualitative and quantitative results. The simulation section includes FEM improvements, porosity mapping, and IGA, reflecting the structure of the methodology chapter for clarity and consistency. The results are presented very briefly, followed by a discussion around the presented results.

Some overall trends could be observed in the testing. This includes drastically lower maximum load and maximum displacement, relative to the initial simulations. A quite large spread in both force and displacement between test specimens was also observed. No observable significant difference can be seen between the different alloys and the spread has to be explained by a different phenomenon.

In the results gradual improvements are presented, and lastly a collection of the most promising methods of simulation are shown, together with calculated errors for force, displacement and absorbed energy. Standard deviation has also been calculated for the test results and is presented.

4.1 Physical testing

Physical test results are divided into quantitative and qualitative results. The qualitative results includes fracture surface examinations and CT-scan results, while the quantitative part includes the force-displacement graphs obtained from the three point bending tests.

4.1.1 Quantitative results from Physical testing

The force-displacement results from physical testing are presented in Figure 4.1a along with color coding based on batch type in figure 4.1b.

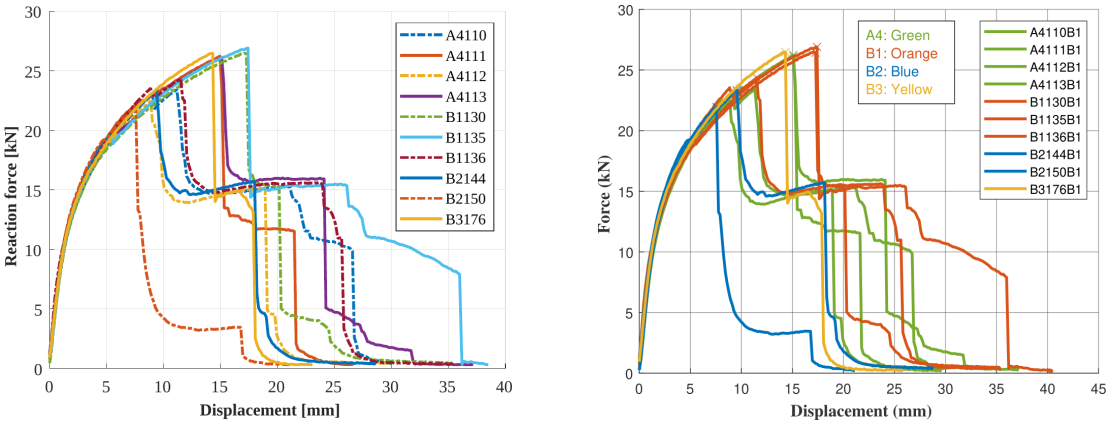

(a) Force-Displacement curves from experiments

(b) Force-Displacement curves colorcoded based on casting batch

Figure 4.1: Characterization of hardening and failure for the physical tests

Table 4.1: Categorization of Failure Types and Colors

Failure sequence	**Beam**
314	A4-111-B1, A4-112-B1, B1-130-B1
31*4	A4-113-B1, B1-135-B1, B1-136-B1, B2-144-B1, B3-176-B1
341*	B2-150-B1

The energy absorbed per beam is shown in Figure 4.2.

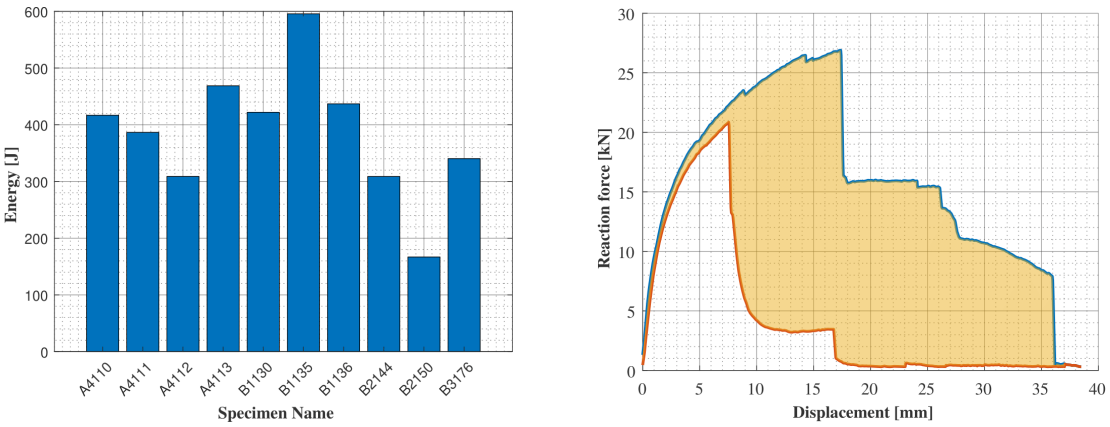

(a) Absorbed energy for each specimen

(b) Largest difference in absorbed energy

Figure 4.2: Difference in absorbed energy

The color coded failure points are plotted in Figure 4.3.

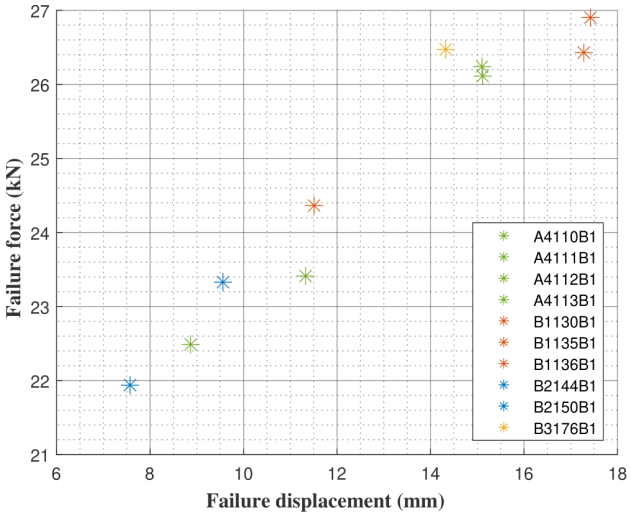

Figure 4.3: Colorcoded failure strain points

The plots above made use of the force displacement curves in an attempt to characterize the behavior of the beam as it was subjected to loading by dividing the data based on: *type of observed failure, absorbed energy, hardening curves* and *failure displacement*. It should be made very clear that 'displacement' is always the displacement of the impactor from the moment of contact, and the same is true for all the simulated results for force versus displacement. As can be seen in Figure 4.1a there is a large spread both in failure strain as well as the behavior after the initial fracture. There were also differences in where the fracture was initialized. In all beams the failure was initiated in the middle rib, but where the first major failure occurred differed between the samples. The graphs clearly show when different parts of the beam fail, indicated by large drops in force coinciding with flange failures.

The order at which the different parts in the beam fail is important because it may be linked to where imperfections exists and perhaps the level of porosity. A working theory is that if an imperfection, such as a pore, is located in a crucial load bearing area, it can cause the beam to fracture sooner and change the character of the rest of the force-displacement curve. Grouping the specimens by failure type produces Table 4.1, further emphasizing *B2-150-B1* as an outlier in both failure type and force-displacement response since it was the only beam where the back flange failed first and it has by far the lowest force-displacement curve. The failure sequence is the order which parts of the beam failed according to the beam anatomy in appendix A where '*' indicates an off-center fracture. The failure 314 means the middle rib fails first, then the front flange then the backflange.

By integrating the curves in Figure 4.1a the energy absorbed by each beam specimen can be extracted and gives a further dimension to the relatively significant spread in the data. It's an interesting metric of comparison especially in the context of crashworthiness of the material, which should ideally absorb as much energy as possible. It should then be noted that the best performing beam absorbed more than twice as much energy as the worst beam in this load case.

The most obvious similarity across the specimens is of course the hardening curve. [1]There is, however, enormous spread in the failure strain as seen in Figure 4.3. This also explains that the spread in energy absorption is of course from the scatter in failure strain rather than hardening behavior. Besides the elastic and plastic stress-strain relationship, the force plateau after the first failure is present in all specimen besides *B2-150*. All beams except *A4-111* reach a very similar force, even though the displacement at which this occurs differs.

A final note on the force displacement curves as an analysis of whether level of recycled material has an influence on material behavior, in accordance to the second objective of this investigation. The batches themselves have been color coded in Figure 4.1b and there is nothing obvious in these plots that could discern one batch from another. From looking at energy absorbed, hardening curves and failure points it is still not clear whether the recycled *B1* material performs better or worse than the primary *A4* material, nor is it clear that the increased levels of iron and vanadium in batches *B2* and *B3* have obvious effects either. The best performing beam consisted of recycled material (*B1135B1*) not primary material and even the primary material shows quite a large spread in energy absorbed and failure points. This means that the most 'reliable' material still exhibits large amounts of unpredictable scatter and did not outperform any of the other batches. Statistical tools were implemented (Appendix: C) and it was found that there were no statistically significant outliers considering energy absorbed, failure displacement and failure force. This further emphasizes a general homogeneity in the batches and that random scatter overshadowed correlations between batches and material properties. One conclusion that can be drawn from this is certainly that it's impossible from this rather limited sample size to say whether and to what extent recycled material and increased levels of iron and vanadium affect material response by looking at force versus displacement plots. It is instead more likely that the casting parameters themselves are causing more spread in the data than what can be attributed to the batch. This claim is further supported by the tests done in the parallel thesis work at VCC that is analyzed and discussed in 4.6. One could argue that the beam with ID *B3-176-B1* displays slightly higher hardening than other beams, something that was also observed in tensile testing results by parallel thesis work by J. Yang and N. Teja[19].

4.1.2 Fractography

An image showing the fracture surface of beam *A4-111-B1* is presented in Figure 4.4

[1]It should be noted that the term 'hardening curve' is slightly misleading. Only some elements experience hardening in this non-linear section since this is on a component level; some elements may even already have failed for this 'hardening'

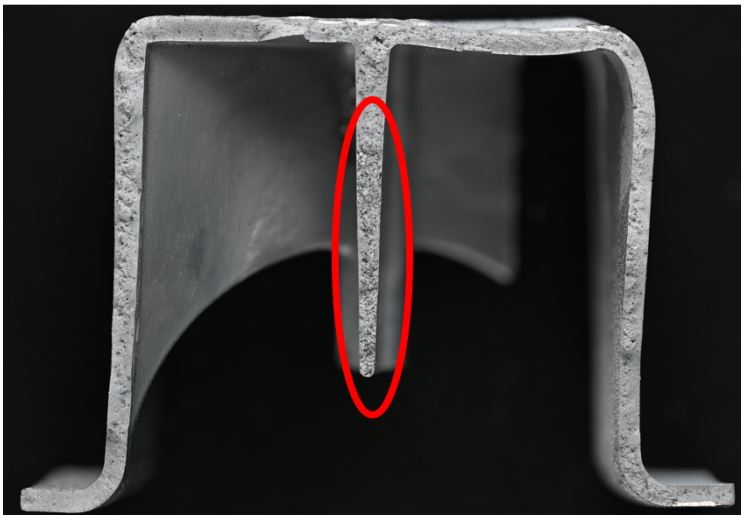

Figure 4.4: Fracture surface of specimen A4-111-B1

The examination of the fracture surfaces (e.g. Figure 4.4) provided valuable insights into imperfections in the components. A band of pores can be seen along the midsection of the beam and particularly clustered in parts of the rib. In fact, the material in the center rib (red) was deemed to be of such low quality, due to the level of porosity, that this part might not contribute to the overall strength of the component at all, according to an expert on the matter[15]. The high density of pores in this area is thought to be a consequence of the release agent used as well as other process related parameters such as low pressure and bad vacuum. The release agent is injected into the mold before the metal melt, and in the sections of higher flow, the agent is flushed away. In the cavity that is the central rib, however, the agent is trapped and, once heated by the melt, it evaporates, causing gas entrapment and pore formation. Similar results were obtained from the fractography conducted on 4 other beams as listed in table 3.2. Based on this knowledge, an intermediate step was taken between the geometrical improvements and the mapping of process-induced imperfections. This intermediate step involved removing elements in the regions with the most prominent porosity and reviewing the effect on the strength of the component, as referred to in chapter 3.3 as *poor man's mapping*.

4.1.3 CT-scan results

The porosity measured by the CT-scan can be seen in Figure 4.5.

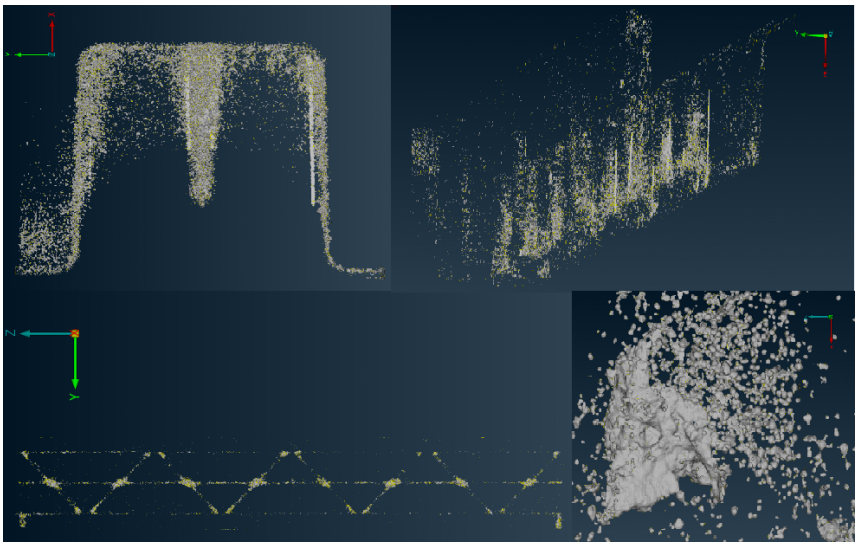

Figure 4.5: Porosity from CT scan

The porosity frequency for lower and higher resolution can be seen in figures 4.6a and 4.6b respectively.

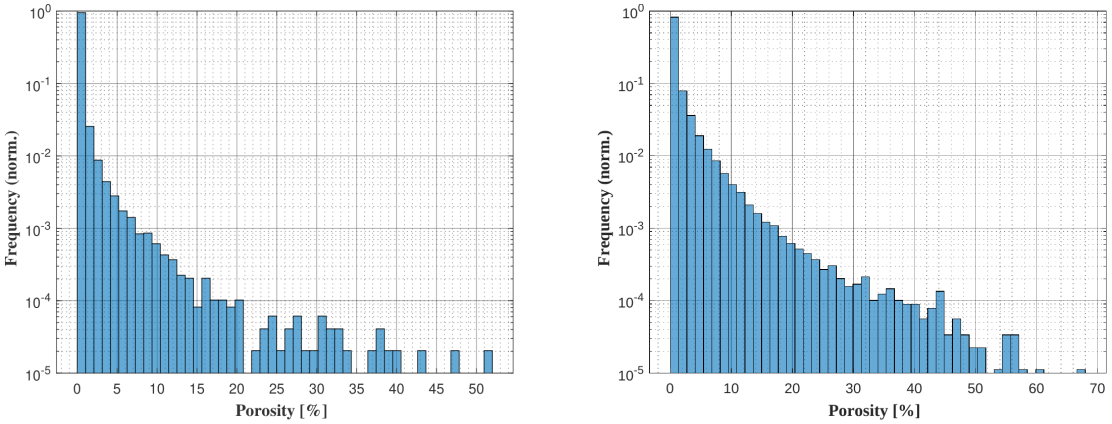

(a) Lower resolution/larger voxel size **(b)** Higher resolution/smaller voxel size

Figure 4.6: Logarithmic relative frequency of porosity volume fraction, log-scale

Firstly, the fear that the beam *A4*-102-B1* might not be representative was alleviated by the three point bend test that can be found in appendix B. The results from scanning the beam confirmed in large part the observations from the fractography in the sense that the beam was significantly porous. This caused a higher emphasis to be placed on mapping porosity, out of all process parameters. From the first CT scan of the beam a total void percentage of 0.2687% was recorded. Mapping this to the CAE mesh led to a total void percentage of 0.2100%, indicating some loss of data but that the mapping and interpolation is still quite good. After increasing the resolution of the CT-scan, a void percentage of 1.0459% was seen for the mapped CAE mesh, indicating the observed porosity is quite dependent on how closely one looks for the pores. In other words, some information is lost from mapping and some information is lost just based on the resolution of the CT-scan which might mean

that the real material is worse than what the scans indicate and what the model can account for. From the previous thesis done on representative volume elements [1] as well as studies done with the GTN model [13][14], this level of porosity could explain the scatter observed in the physical results 4.1a both for yield and strain magnitudes at failure.

For further analysis, the porosity distributions were plotted in histograms (fig 4.6a). It is clear first of all that the vast majority of the cells have between $0 - 10\%$ void. Interestingly, when the resolution of the CT-scan was increased, both the average and maximum porosity fraction increased, and the portion of cells containing little to no porosity reduced. The fact that the smaller pores could not be captured with the larger voxel scan suggests that there might be even smaller pores present that can not be captured with even the refined CT-scan. Noteworthy is that the grid size does not effect the porosity fraction, since the grid is only used for aggregation. The grid mesh size as well as the solid tetra geometry mesh does however seem to influence the porosity volume fraction distribution in the receiver mesh. The higher resolution scan does have a draw-back when it comes to mapping, namely that since the entire beam could not be scanned, the beam section has to be extended by copy-pasting to make mapping possible.

4.1.4 Miscellaneous test results

Imperfections found in test specimens are shown in figures 4.7a-4.7c.

(a) Visible damage from ejector pins

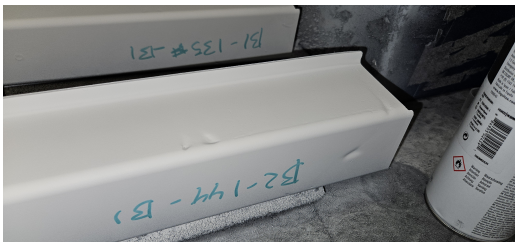

(b) Dents in beam side and roof

(c) Surface porosity

Figure 4.7: Examples of physical surface imperfections observed in beam testing

It was noticed that the test samples received from the supplier included some imperfections both in the form of surface holes and dents. The surface holes can be found mostly in the crevice where the center and converging rib meet at the ejector pin. Dents can be observed in both A and B side flats near the roof, as well as ejector dents in the flanges. The ejector dents also coincide with the center of the beam, as well as the location of the crack. These were not considered for the CAE model in the coming chapters.

4.2 Investigation of geometry and element formulations

As mentioned in the method chapter, the order of the results presented are made to reflect the steps that were taken to get the simulated results closer to the physical results. First a baseline of the different material cards was established, then the mesh sensitivity was studied for shells and solids and geometry improvements were made based on a 3D scan and measurements. A new geometry is established which is then used in efforts made to map process parameters to the CAE model and scale material cards.

4.2.1 Baseline simulation results

Baseline simulations results are shown in Figure 4.8.

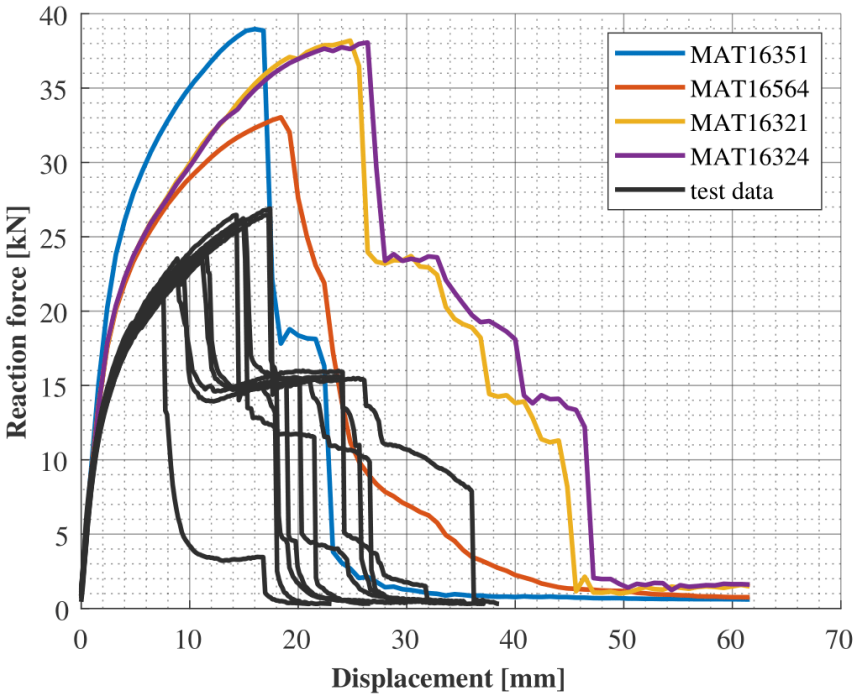

Figure 4.8: Baseline simulations

Failure sequences for base simulations are shown in table 4.2.

Table 4.2: Failure sequence as function of material model

Material card	Failure sequence
MAT16321	134
MAT16324	134
MAT16351	1*34
MAT16564	314

To provide a baseline for further investigations, some material models using the coarsest mesh have been plotted together with the test results. The material models used are MAT16351 developed by Dyna, MAT16564 developed at VCC and Crach-FEM cards MAT16321 and MAT16324. The mesh size used was a target length of $3.4mm$.

The simulations seem to overpredict both the stiffness, maximum force and the displacement until failure. The solid simulations seem to more accurately model the first failure but none of the models seem to be able to capture the plateau after the first drop which can be seen in most tests. Interestingly, the material models differ from the physical testing in the type of failure that is found as seen in Table 4.2 if one is to compare it to Table 4.1.

For the mesh sensitivity study, only the material cards MAT16351 and MAT16321 will be showcased for brevity. After convergence was found, that mesh refinement was used for MAT16564 (solid element card) and MAT16324 (shell element card) as well.

4.2.2 Mesh sensitivity

Results from mesh convergence study for shell elements is shown in Figure 4.9.

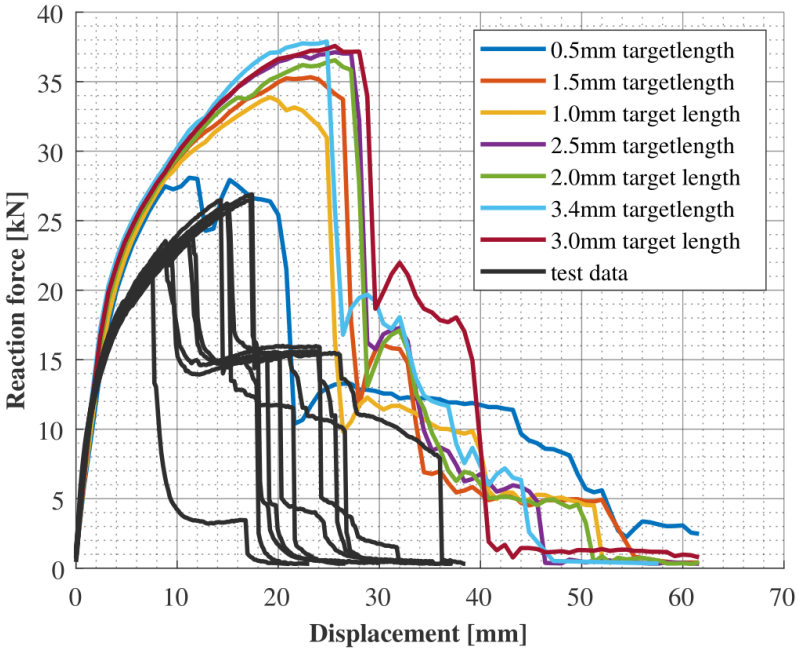

Figure 4.9: Mesh sensitivity study for shells MAT16321

Max force and absorbed energy diagrams are shown in figures 4.10a and 4.10b respectively.

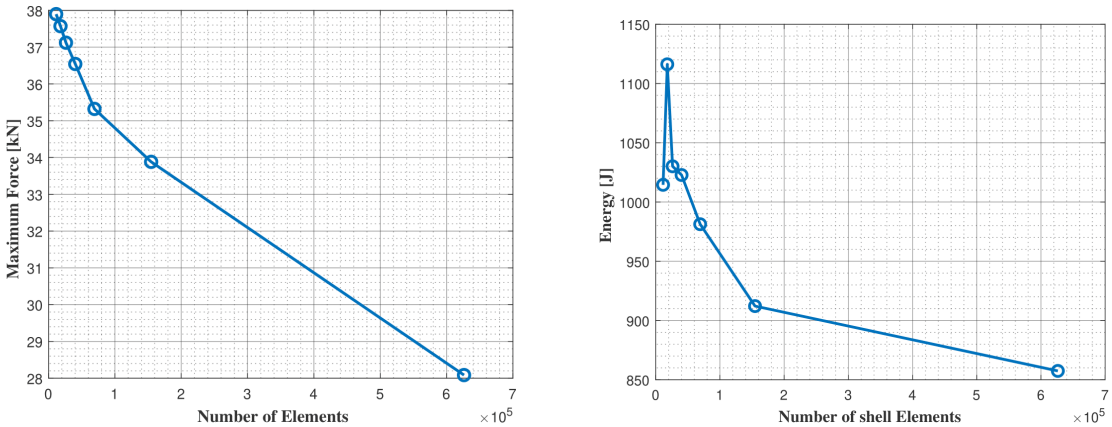

(a) Max force study **(b)** Energy study

Figure 4.10: Convergence study, shell elements, MAT16321

Simulation time versus element count is shown in table 4.3.

Table 4.3: Mesh sensitivity analysis for shell elements

Mesh size [mm]	Time (seconds)	Number of Elements
3.4	52	11433
3.0	67	17979
2.5	85	26227
2.0	114	40268
1.5	187	69200
1.2	264	109607
1.0	368	154634
0.8	583	243435
0.5	1697	626285

Results from mesh convergence study for solid elements is shown in Figure 4.11.

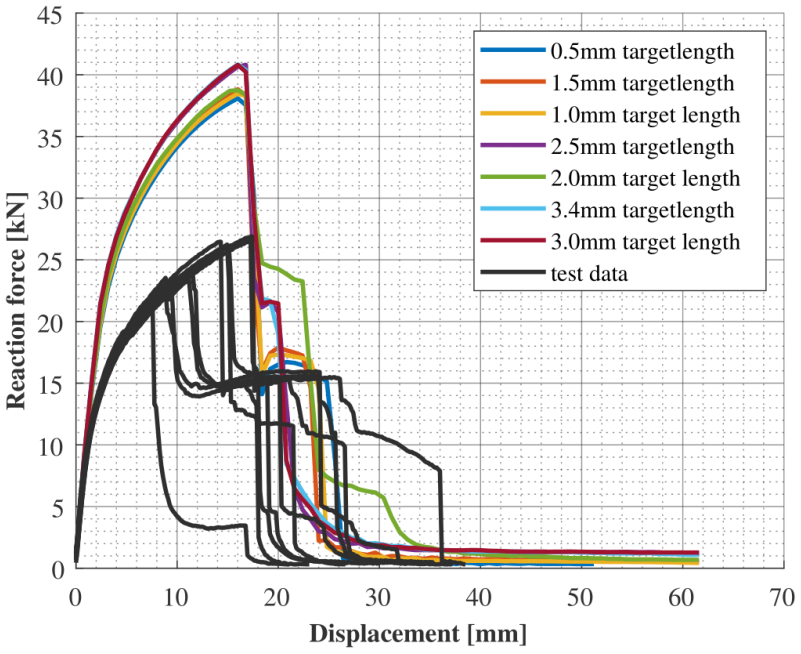

Figure 4.11: Mesh sensitivity study for solids MAT16351

Max force and absorbed energy diagrams are shown in figures 4.12a and 4.12b respectively.

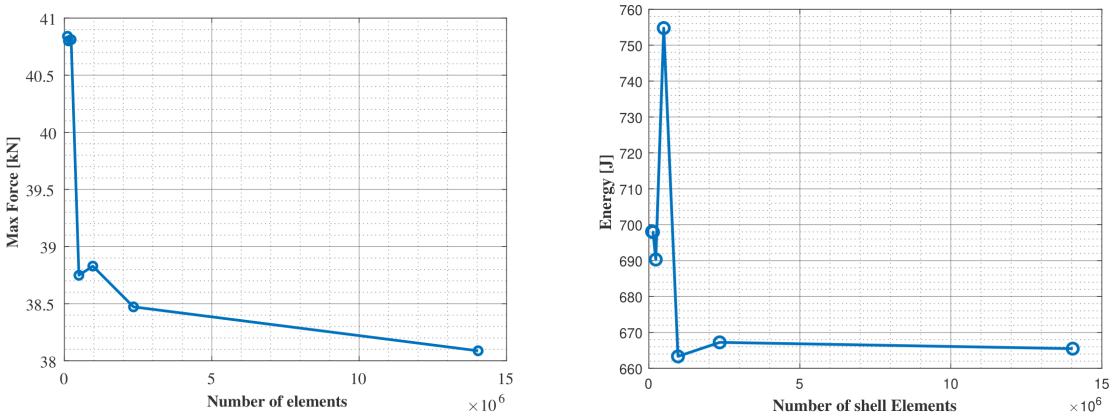

(a) Max force **(b)** Absorbed Energy

Figure 4.12: Convergence study, solid elements, MAT16351

Simulation time versus element count for solid elements is shown in table 4.4.

Table 4.4: Mesh sensitivity analysis for solid elements

Mesh size [mm]	Time (seconds)	Number of Elements
3.4	341	104701
3.0	423	136783
2.5	626	228878
2.0	1040	492222
1.5	1488	963973
1.0	3390	2344624
0.5	50715	14036537

For further investigations of solid elements a target length of 2 mm was used since it was regarded as a good middle ground between accuracy and computational cost, as well as it was deemed to have converged. The maximum force as well as the fracture strain seem to be captured when it comes to solid elements. For shells the 1.5 mm target length is used, though in the case of shells it is not as easy to say which element size is the most rational to use going forward since it did not converge in the same fashion as the solid mesh. It was observed that for very refined shell elements contact issues started to arise that were non-physical, seen in the 0.5 mm target length plot in Figure 4.9. Although it aligns rather well with the results, shells eroded and oscillated in non-physical manners on the contact points of the supports. Attempts were made to resolve this issue by controlling the added mass for the explicit solver by reducing the time step threshold for when mass is to be added. Sometimes too much added mass will give contact issues and so allowing for smaller time steps will slow the simulation in an attempt to make it more stable but this gave no improved results.

4.2.3 CAE Geometry Modification

The results from the geometrical changes to the solid and tetra mesh model are presented in figures 4.13a and 4.13b respectively.

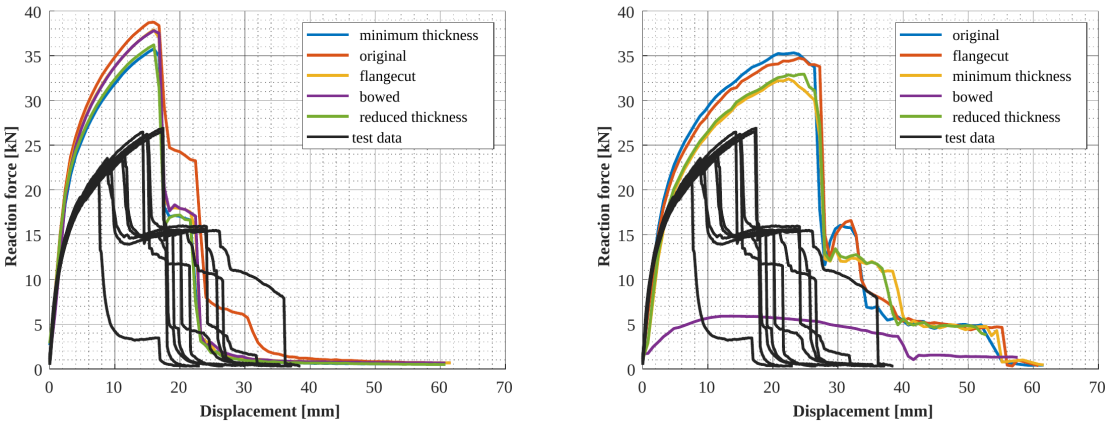

(a) Solid tetra elements, MAT16351 **(b)** Shell elements, MAT16321

Figure 4.13: Geometry improvements

The first alteration made was cutting the flanges, shown in yellow, but partially hidden behind the purple *bowed*-graph in Figure 4.13a. There is a slight reduction in maximum force while the displacement at which that force occurs is not greatly affected. On the other hand, the imitated bow in the beam did not in a significant way change the load-bearing capacities of the component for solid elements. Changing the thickness also lead to a reduction in peak force, but also slightly reduced the displacement at which the peak force was obtained. Interestingly the elastic stiffness did not seem to change much, while the hardening behavior was different. The reduction in thickness is especially relevant to casting processes since shrinkage of the detail during cooling is not uncommon and should be accounted for. Taking the measured average and minimum thickness, shown in green and blue respectively, shows the greatest reduction in peak force compared to the CAD model. The displacement is not reduced as much but is on par with the physical tests. The difference between the average and minimum reduced thickness is close to negligible but non-zero. Given the reduction of the flange width is not very large, 2.728 mm to 2.67 mm, that is to be expected.

As for the shell elements, the reduced width of the flange also reduced the peak force, but also increased the displacement at which the big drop in force occurred. And for the bow it completely changed the failure behavior of the beam, resulting in a force not even close to the physical tests. Moving forward, the average reduced thickness using MAT16351 will be used as a baseline for further investigations. Note that this beam is also flange-cut in line with the geometry modification road map 3.10. Further improvements are studied by themselves, and are unless specified not stacked. As has become evident in the geometry study as well as by taking measurements of the test samples, the geometry of the cast beam deviates from the original CAD. This is far from desirable since in reality CAE analysis will be done on the CAD geometry, and if the cast geometry differs from this it will reduce the accuracy of the CAE results. This further emphasizes issues with the current casting process.

4.2.4 Element formulations

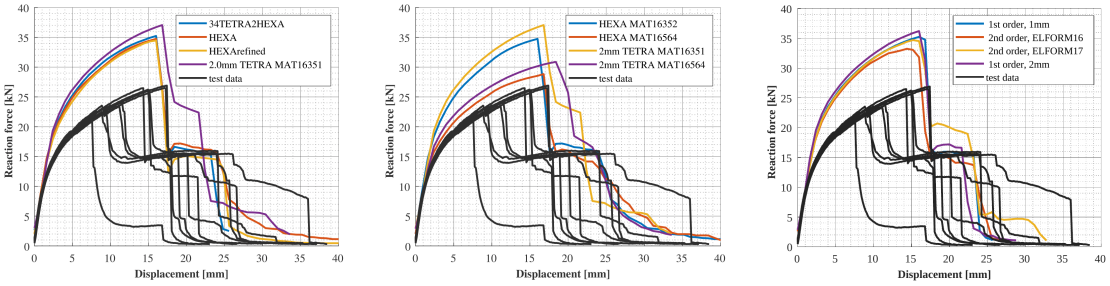

(a) Hex. mesh, MAT16352 **(b)** Hexahedral elements with MAT16564 **(c)** First vs. second order elements

Figure 4.14: Element formulation studies

Simulation time versus number of elements for second order tetrahedral and hexahedral elements is shown in table 4.5.

Table 4.5: CPU timing comparison for different element formulations on 128 cores

Method	CPU Time (seconds)	Number of Elements
HEXArefined	4958	956822
HEXA	367	38248
34TETRA2HEXA	2990	410948
1st order tetra (2mm)	943	458074
1st order tetra (1mm)	3390	2344624
2nd order tetra ELFORM16 (2mm)	3610	458074
2nd order tetra ELFORM17 (2mm)	5905	458074

The material card MAT16564 with hexahedral elements are plotted for absorbed energy and failure displacement compared with physical testing.

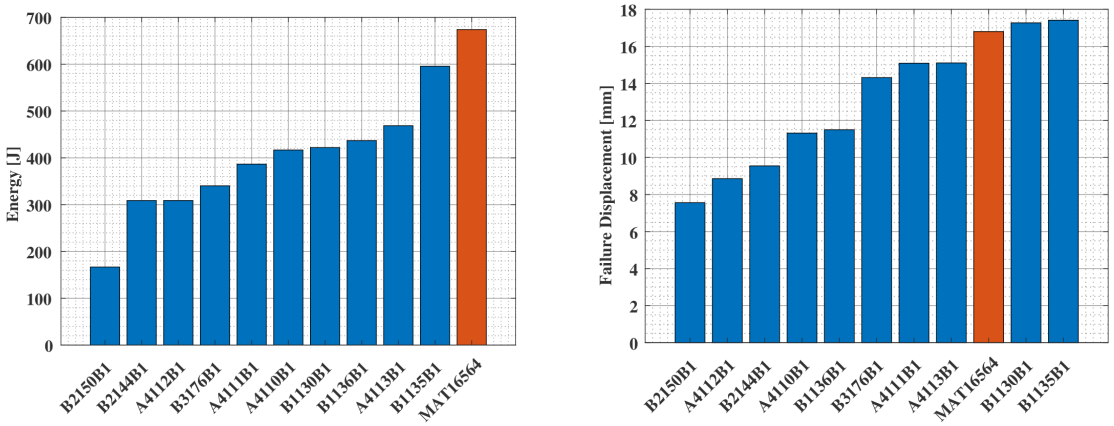

(a) Energy absorption **(b)** Failure displacement

Figure 4.15: Comparison between physical data and HEXA MAT16564

The results from the two hexa-meshing techniques can be seen in Figure 4.14a, namely the manually constructed hexahedral mesh (HEXA), including the refinement of the same (HEXArefined), and the automatic hex-meshing routine that converts tetra-elements to hexa-elements (34TETRA2HEXA). Meshes of these beams are showcased in Figure 3.7. The curves match one another, and the other solid element formulations. The force is still much higher than the physical results however the failure strain is reasonable, indicating that the material response is still too stiff. The other result is that it is hard to justify the time investment needed to manually create the hexagonal mesh. For CPU timing in table 4.5 it is clear that the manually created mesh is much faster on account of having much fewer elements but took more than 1 week to construct the mesh itself manually. If one were to scale it up to the full part that is to be megacast, it would be infeasible. Another finding is that creating a hexa mesh from an already existing tetra mesh is an efficient way of reducing the amount of shear locking which can otherwise be a problem with tetra elements.

In Figure 4.14c there is a clear difference between first order and second order tetrahedral element formulations. As expected the simulation takes about 4 times as long to compute. By only looking at the max force this means an increase in computational time of 400% to reduce the max force by around 8%, while another 21% reduction would be required to match the observed physical results.

As expected from the baseline set in Figure 4.8, MAT16564 exhibits a much lower force-displacement curve than the LS-Dyna developed MAT16351 and MAT16352 cards and as seen above (Figure 4.14b) the same is true for the hexahedral element types. Thus far, without considering any process parameter mapping, *HEXA MAT16564* is performing most accurately with a force peak of around $29kN$ compared to the highest test result of around $27kN$ at a nearly identical displacement of the impactor (16.8 mm vs. 17.4 mm). Figures 4.15a and 4.15b showcase that both the energy absorbed and the failure displacement point fall within the range of the physical tests.

It is evident that the improvements in geometry, element formulation and modeling techniques cannot alone paint the entire picture since the simulations across the board are relative to the physical results. Therefore it is essential to investigate what other phenomena impact both the load-deformation relationship and the failure behavior. After examining the failure surfaces, the most logical next step is to investigate how imperfections caused by manufacturing can be included in the model.

4.3 Mapping

This section presents results from as well as discussion around mapping in the order following order: *Macroscaling, Porosity meshing, Failure surface and Hardening curve scaling* and *Microscaling.*

4.3.1 Macroscaling: Poor man's Porosity Mapping & Homogeneous scaling

In Figure 4.16 beams with PMM are compared to their normal counterpart for solid elements.

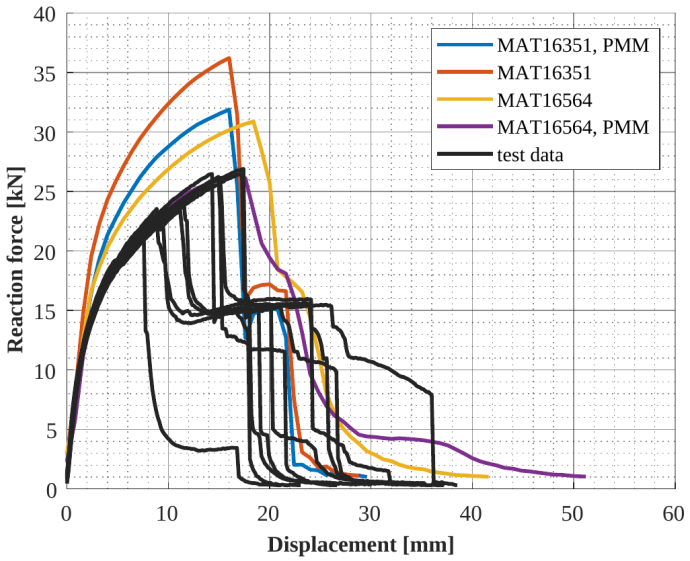

Figure 4.16: Poor mans mapping against new baseline for solid tetra elements with material models MAT16351 and MAT16564

Figure 4.17 shows the effect of a reduced rib for shell elements.

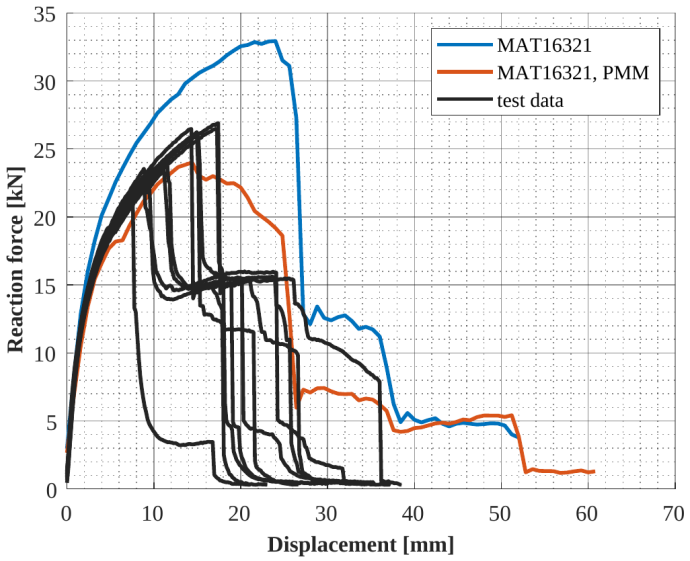

Figure 4.17: PMM against new baseline for shell elements with material model MAT16321

The homogeneous scaling of the hardening curve for shell and solid elements are presented in Figure 4.18.

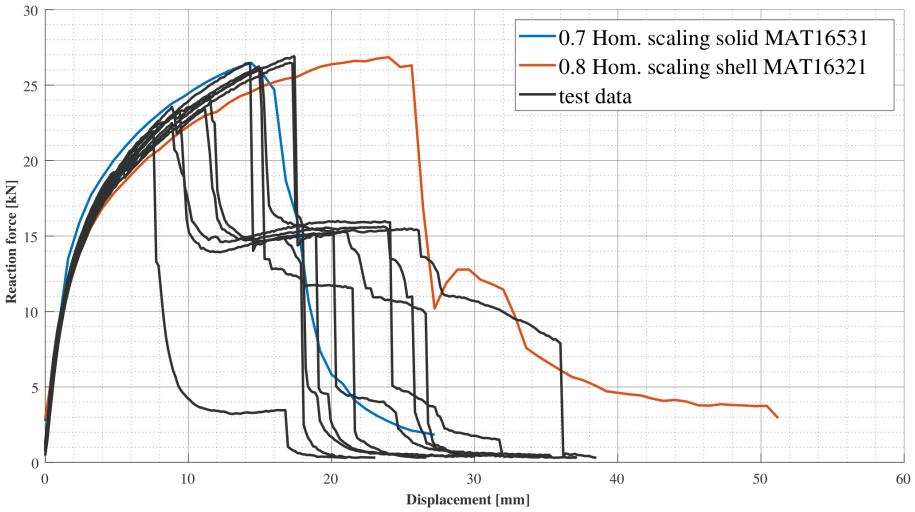

Figure 4.18: Homogeneous scaling of the hardening curve for MAT16351

Note that the graph for MAT16564 with removed center rib is partially hidden behind the test results in Figure 4.16. The initial failure corresponds very well with the best performing test sample (*B1135B1*). While removing the rib can account for some of the reduced force in testing vs. simulations, the fact that MAT16451 with reduced center rib is still higher than the test results suggest it is of interest to keep investigating what can help explain the further scaling needed to achieve the same behavior as MAT16564.

When the PMM is applied to shells the same pattern emerges as could be seen in the geometry study. Shell elements react very dramatically to geometry changes. The hardening curve does not match the test results and the behavior after the first fracture is not representative. It is not surprising that shell elements do not perform well since a lot of the geometry features get lost when going from solid 3D to shells.

As a final note on this macro scaling investigation, it was noted that one would have to scale down the hardening curve of *MAT16351* by almost 30% in order for it to fit the test data as seen in Figure 4.18. For the shell elements in *MAT16321* one needed around 20% scaling to achieve a similar hardening curve (and the failure strain should preferably also be scaled). Usually the fracture modelling is the intricate part of simulating loading until failure, *not* the hardening curve. The fact that one has to scale by up to 30% indicates that the material that is being used in this investigation is performing *much* worse than what these cards were calibrated for, and it should be noted again that *all* material cards used in this investigation were calibrated for the exact aluminium alloy that was tested on, though it was a different part cast with a different tool. Thus if the material is chemically identical, and the physical tests showed no significant disparity between level of recycled content then it is very likely that the material properties that were observed are caused by the casting production process itself.

4.3.2 Porosity meshing

The inserted pores from the CT scan simulated with MAT16351 and MAT16564 produced the results in Figure 4.19.

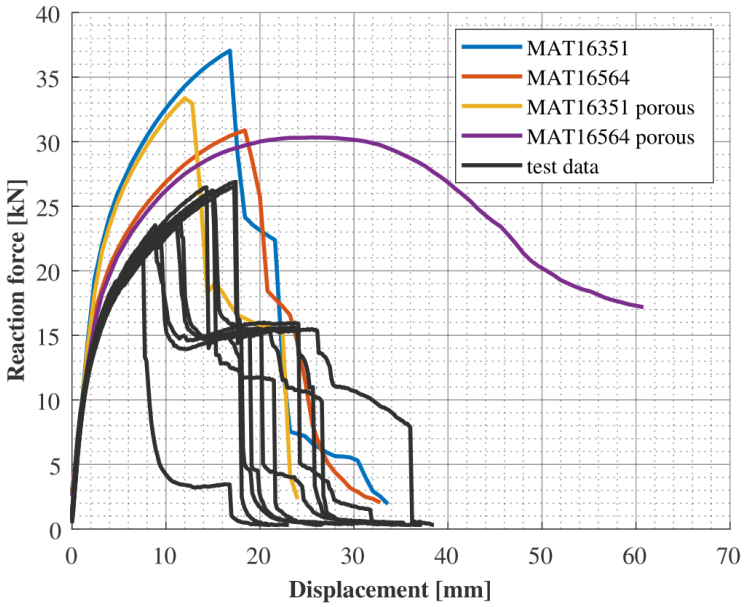

Figure 4.19: Porosity meshing result

The first thing to note is the strange result from *MAT16564*, which becomes less strange when considering this material card already has applied scatter. In other words the card has been scaled in hardening and failure strain with a random scatter function on an element basis, and so applying pores to the material is in a way accounting for imperfections twice. The second thing to note is that it did not make a very big difference to *MAT16351* which does not have any scatter. This could mean that the wrapping method to make the pores more coarse is not accurately capturing their behavior or that the CT scan does not catch all the pores. If the effect of these first two are negligible then it could mean that porosity alone does not account for the reduction in stiffness. Regardless of the case, it further discredits a method that was questionable to begin with. Firstly it is extremely computationally expensive and secondly it relies on a CT scan of the entire component, and both of these reasons would of course make the method infeasible on larger components, like the megacasting floor.

4.3.3 Failure Strain and Hardening scaling for porosity void fractions

In the Figure below, 4.20, the RVEs with their respective percentage of voids are plotted.

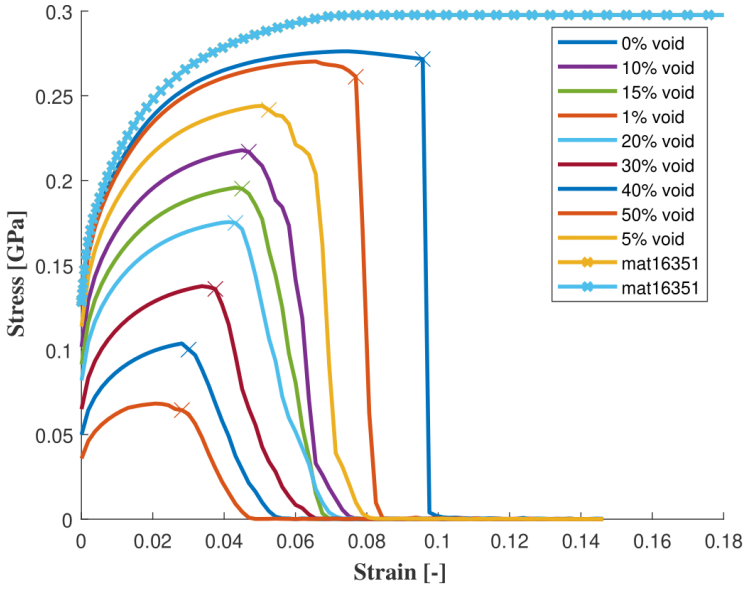

Figure 4.20: Hardening curves and failure strains for RVEs with macropores MAT16351

The resulting scaling factors for hardening curves and failure strains are presented in table 4.6.

Table 4.6: Void factors and corresponding scaling factors

Void Factor	σ_Y **[GPa]**	ε_f**[-]**	**Hardening Scaling**	**Strain Scaling**
0.0000	0.1289	0.0957	1.0000	1.0000
0.0100	0.1017	0.0769	0.9736	0.8040
0.0500	0.0913	0.0525	0.8822	0.5492
0.1000	0.1255	0.0469	0.7889	0.4904
0.1500	0.0819	0.0450	0.7081	0.4708
0.2000	0.0650	0.0432	0.6352	0.4512
0.3000	0.0499	0.0375	0.5040	0.3923
0.4000	0.0358	0.0300	0.3870	0.3139
0.5000	0.1137	0.0282	0.2780	0.2943

The scaled RVEs are compared with their meshed pore counterparts in Figure 4.21.

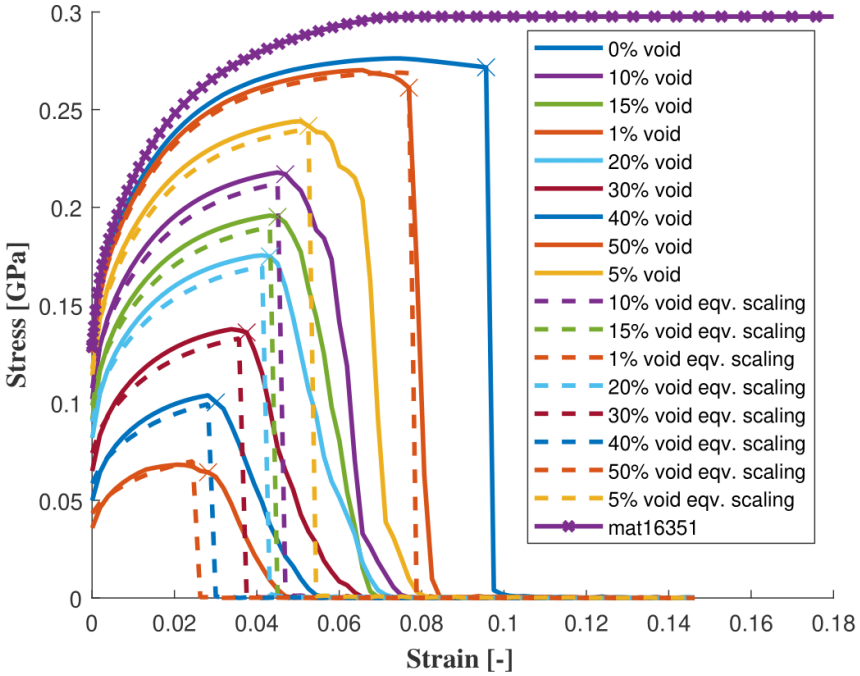

Figure 4.21: RVEs with meshed pores vs. RVEs with equivalent scaling

The RVE scaling technique used in this investigation is validated via a comparison to [1] in Figure 4.22.

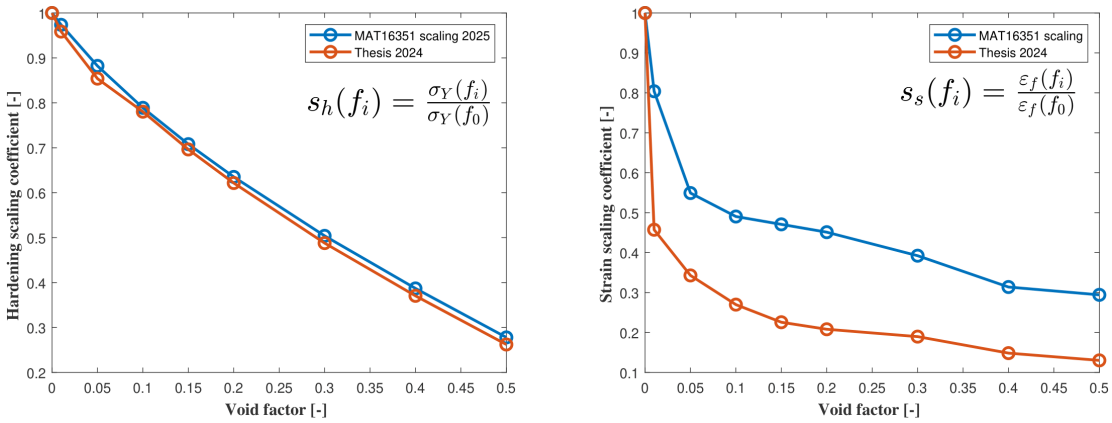

(a) Hardening scaling **(b)** Strain failure scaling

Figure 4.22: Comparison of scaling curves made from Coric and Seyedraoufi (2024)[1] and this investigation (2025) for the same aluminium alloy

It is clear that both hardening curves and failure strain are correlated to the void fraction as seen in Figure 4.20 and should thus be scaled as described in the method chapter 3.3.3. Since material card MAT16564 already applies scatter scaling, only MAT16351 was tested with RVEs in order to avoid double scaling. Scaling is done through the equations 3.1 and 3.2 and tabulated in 4.6. When these tabulated scale factors are used for equivalently scaled RVEs they compare very well to their real meshed pore counter parts in 4.21. This indicates that at least on an RVE level

(which corresponds to an elemental level) is is possible to achieve the material response roughly equivalent to that of an inserted pore by simply scaling hardening and failure strain.

Since this methodology was inspired by Coric and Seyadroufis thesis in 2024 [1], a comparison was made to insure validity of the approach. While both material models (MAT16351 and the material in [1]) are calibrated for the exact same alloy, their samples were taken from different cast components. Despite this, the way the material reacts to the presence of pores is very similar, as can be seen in the scaling plots from Figure 4.22. In other words, the pore size correlation to hardening and failure strain seen from [1] is very similar to the trends seen in this investigation. The tabulated data in 4.6, having ensured validity to a reasonable degree, were then applied to the PSDM and CTM methods.

4.3.4 Mapping from process simulation data (PSDM)

A histogram of pore size frequency was plotted from the porosity data from *ProCast* in Figure 4.23.

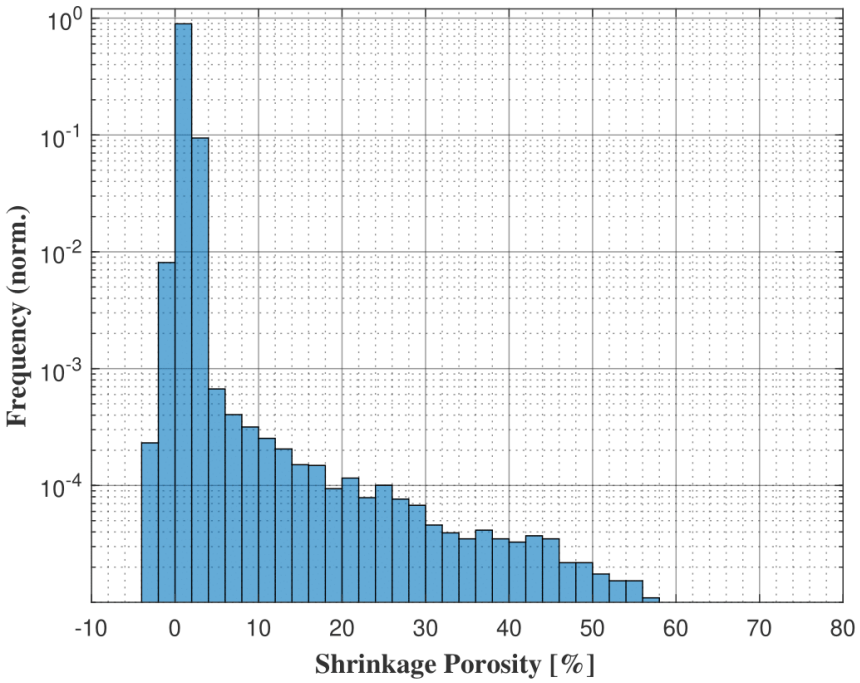

Figure 4.23: PSDM porosity histogram

A cross section of the porosity fringe plot after mapping PSDM and CTM data is shown in Figure 4.24.

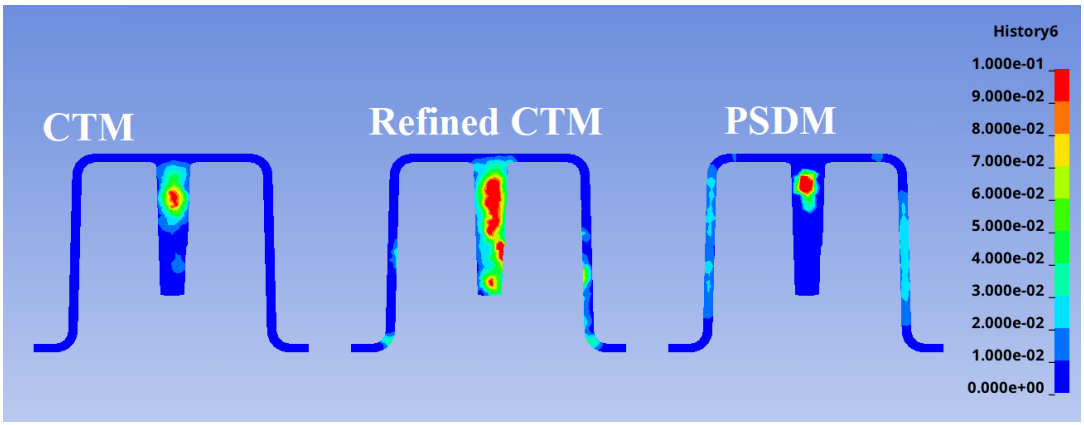

Figure 4.24: CTM, Refined CTM and PSDM porosity

The results of mapping the *ProCast* casting simulation data is shown in Figure 4.25

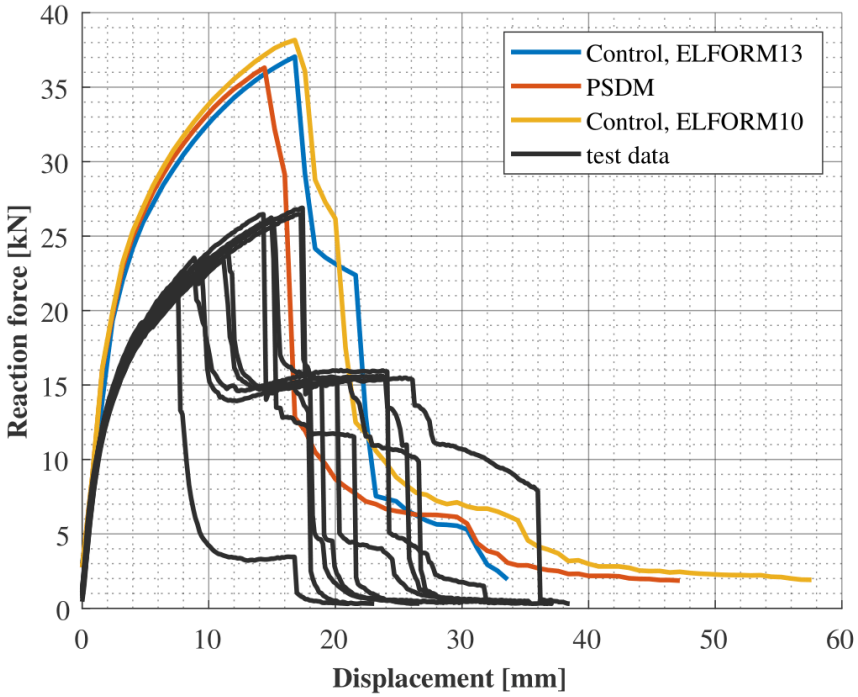

Figure 4.25: Mapping results for PSDM for scaling of failure strain and hardening curves

Some validation of the PSDM was first conducted to ensure that it gave the same general behavior as the CT scan. Note of course that the casting process can vary so the exact placement of pores cannot be expected to be the same between CT scans and casting simulations. Thus a histogram of the pore frequency was produced and compared to the CT-scan histogram in 4.6a where a similar behavior of the pore size distribution can be seen. However, there are certain indications that the PSDM data is not entirely reliable, eg. negative values in shrinking factors are observed. Another key difference is that the higher levels of porosity (over 10%) are much lower in the PSDM data even if the nature of the pore distribution is similar in

both mapping techniques as seen in Figure 4.24. In Figure 4.24, the cross-section at an arbitrary but illustrative point, shows the typical behavior seen throughout the beam. The general behavior is the same throughout the mapping where pores are generally found in the ejector pins of the beam.

When mapping on to the beam it is important to note again that with the current version of the LS-Dyna software, it was infeasible to map history variables to hardening and strain curves with ELFORM13, thus ELFORM10 had to be used. In Figure 4.25 it is clear that even after scaling in accordance to the RVEs no significant improvements were observed. This can be explained by the homogeneous scaling which showed that if *every* element was scaled down 30% for this material (MAT16351) then it would align with the physical data. The elements that were mapped with pores obviously did not equate to this homogeneous scaling and this makes sense since the vast majority of pores are between 0-2% void which is only about a 3% down scaling of hardness according to table 4.6. Less than 1 in thousand pores (according to the histogram) have more than 10% void which is where scaling over 20% is observed.

4.3.5 CT-scan based mapping, CTM

The simulation results from mapping based on the CT scans are presented in Figure 4.26.

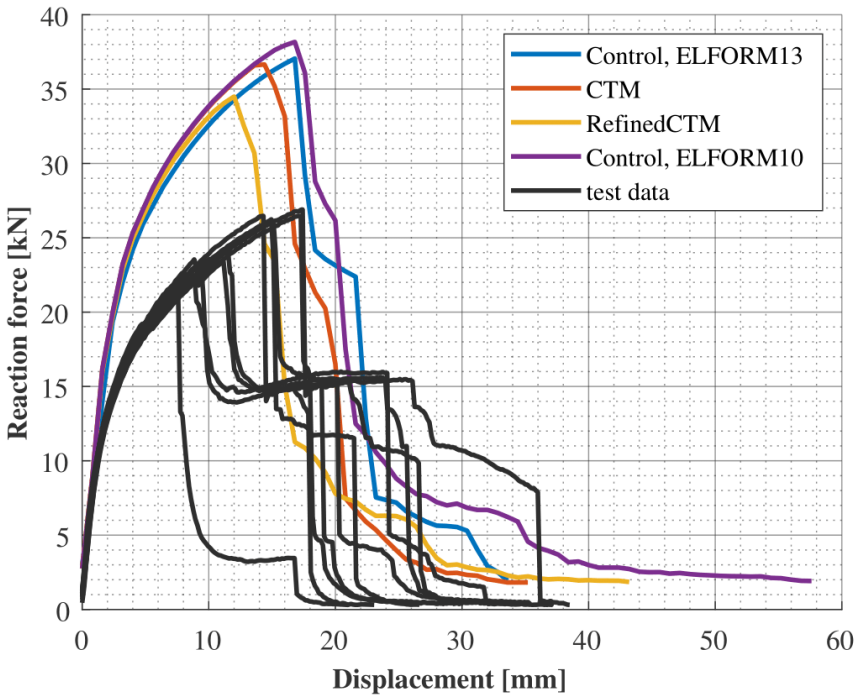

Figure 4.26: Mapping results for CTM for scaling of failure strain and hardening curves

As seen from Figure 4.26 the mapping does have an effect on the simulated result, however, it seems to have more effect on the failure strain than the non-linear part,

which was also seen for the PSDM approach.

It is clear that the refined CT-scan captured more pores, as is evident from the cross section analysis in Figure 4.24, and so the mapping had a larger effect. Still it is clear that mapping is still not quite getting close enough to the physical test results. Indeed, out of all techniques, the porous insertion seems to be 'closest' to the physical results. Since the direct porous insertion and all the mapping techniques still do not quite align with the physical test results, it is hard to claim that porosity is the only factor that play a part in the disparity between the simulated and physical results.

4.4 Isogeometric analysis

In the following sections the results from studies of IGA mesh sensitivity are presented.

4.4.1 Geometry mesh study

The force-displacement curves for different geometry meshes are shown in Figure 4.27.

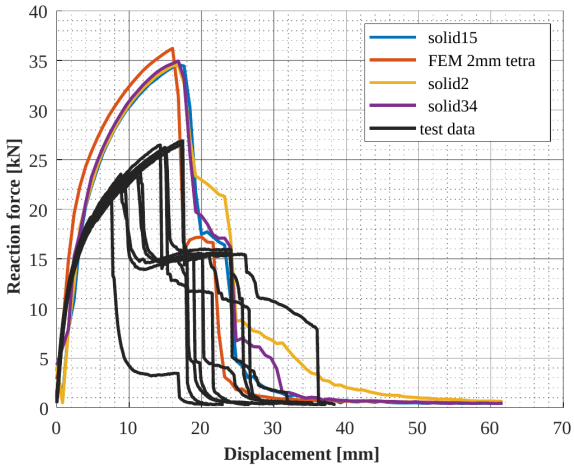

Figure 4.27: Force-displacement for different Geometry meshes

Simulation time is presented in table 4.7.

Table 4.7: Simulation times for different geometry mesh target lengths

Target length [mm]	Simulation time
1.5	1h48min
2	1h22min
3.4	1h08min

Apart from a longer simulation time for more elements the different mesh size target lengths are nearly identical. They all display a slightly reduced peak force but increased maximum displacement compared to FEM.

4.4.2 Background mesh sensitivity

The force-displacement curves for different EELs is shown in Figure 4.28.

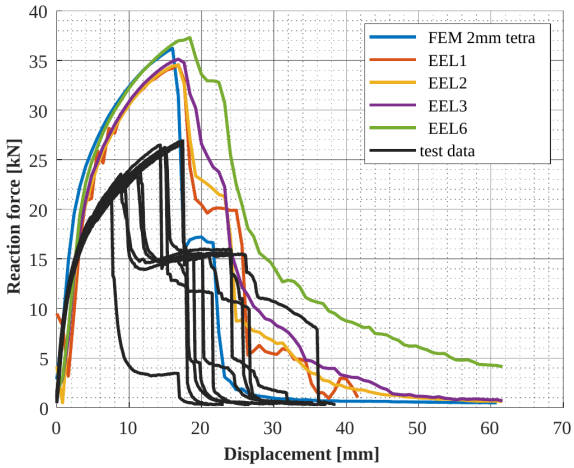

Figure 4.28: Force-displacement for different EELs

IGA visualization problem are shown in Figure 4.29.

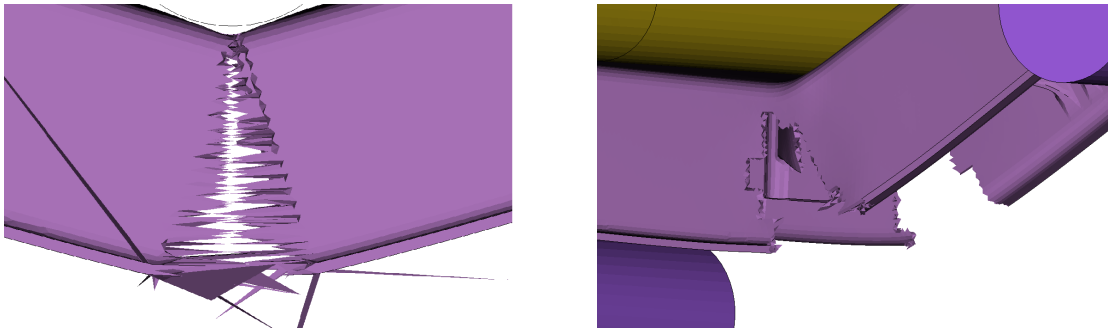

(a) EEL1 **(b)** EEL6

Figure 4.29: Images showing issues with visualization when using IGA

Simulation time versus EEL is shown in Figure 4.8.

Table 4.8: Simulation time for different EELs

EEL [mm]	Simulation Time
1	6h40min
2	1h22min
3	43min
6	38min

Comparison between IGA and FEM stress fields is shown in Figure 4.30.

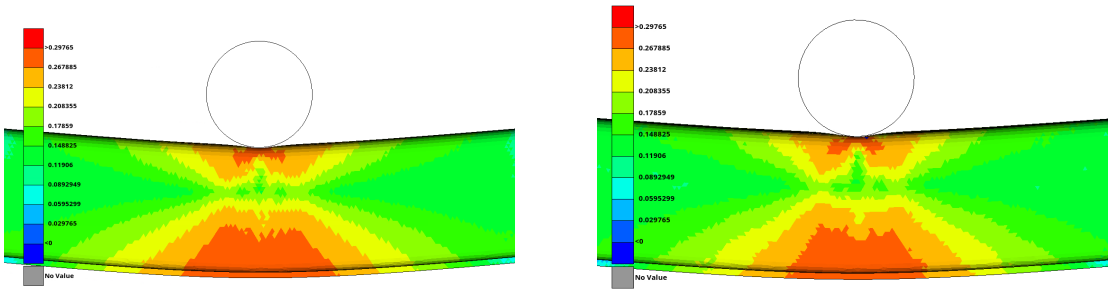

(a) FEM, 2 mm tetra **(b)** IGA, 2 mm tetra, 2 mm EEL

Figure 4.30: Stress field comparison across simulation methods, MAT16351

For the both extremes, EEL 1 mm and 6 mm, we can see some spurious oscillations in the force-displacement curves. Looking at the deformed geometry, problems with visualization are also evident, see Figure 4.29a and 4.29b. The 1 mm EEL has trouble visualizing elements that have been deleted and elements close to deleted elements. The 6 mm EEL shows how elements are deleted in a IGA context. Instead of the geometry solid elements being deleted its the background mesh cells that are deleted, resulting in large sections of the geometry being deleted, and a failure character that differs from the FEM and finer EEL meshes.

Apart from the difference in force-displacement results there is also a significant difference in preprocessing for the differently coarse meshes. The four different EELs and the corresponding simulation times are shown in table 4.8.

The stress field right before crack initiation using the 2 mm target length geometry mesh and 2 mm EEL gives the stress field shown in 4.30b. As comparison, it is shown next to the stress field of the new baseline established in chapter 4.2.3 in Figure 4.30a. Both simulation techniques reach the same peak stress, although the region of the highest stress in the FEM model is marginally larger. Note that it is the stress field that is shown, this since there was trouble showing the strain field when using IGA.

As can be seen both in force displacement graphs and in stress field visualizations, IGA in LS-Dyna shows promise but is not yet mature enough to be a replacement. As of present IGA does not facilitate the same capabilities of customizing material models, for example the material model used in the MAT16564 card is not yet implemented. The creation of the background mesh is also slow.

4.5 Final comparison

A force displacement graph including measures of error with respect to maximum force, energy and displacement is compared for the best performing simulations in Figure 4.31.

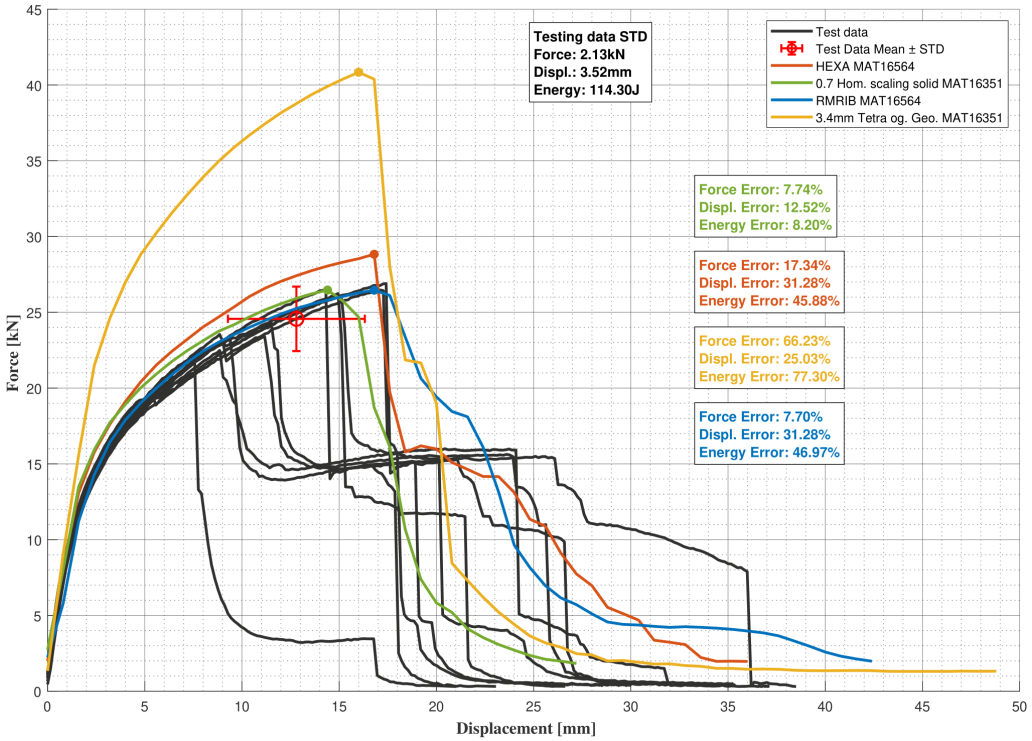

Figure 4.31: Best performing simulation plots and results from the physical tests

A strain field comparison is made for the best performing simulations in Figure 4.32.

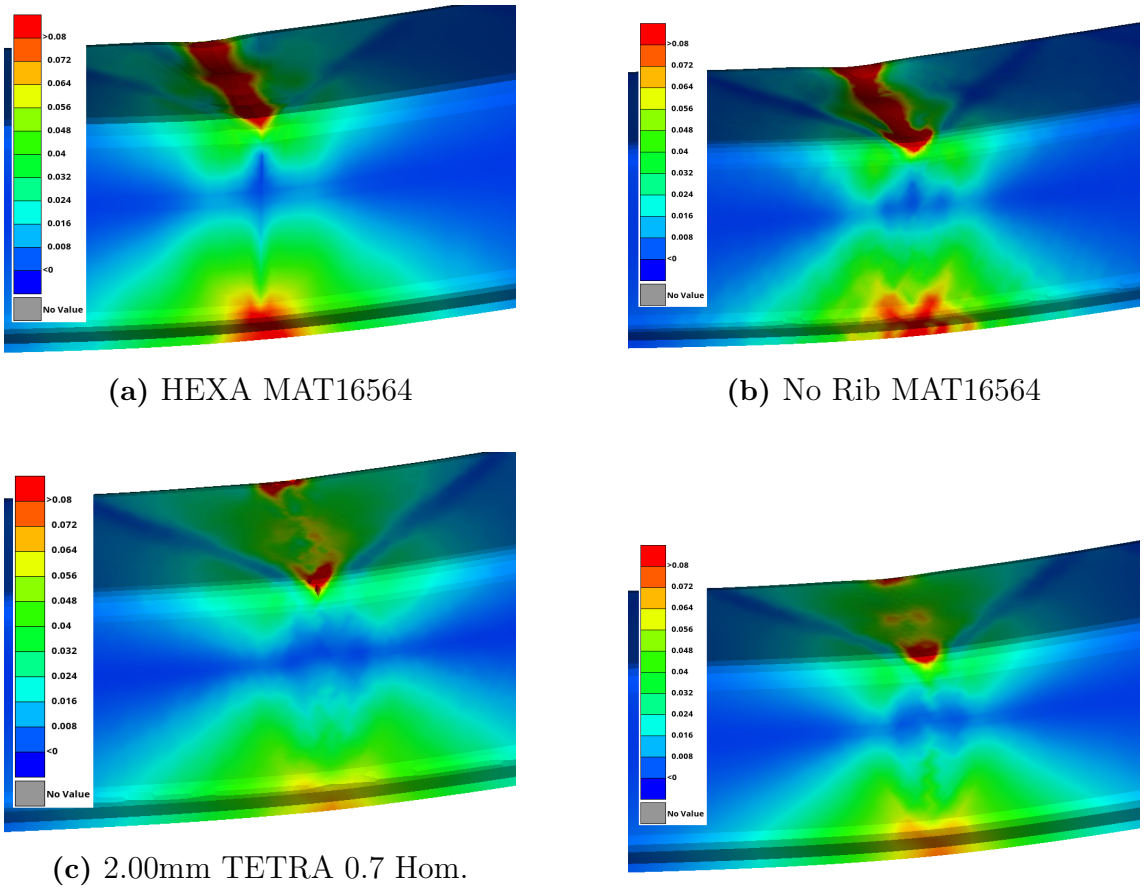

(a) HEXA MAT16564

(b) No Rib MAT16564

(c) 2.00mm TETRA 0.7 Hom. Scaling MAT16351

(d) 3.4mm TETRA MAT16351

Figure 4.32: Strain field fringe plots of best performing simulations (one timestep before initial fracture)

3D DIC data from beam *B1-136-B1*[2] is presented in Figure 4.33 and 4.34.

[2]B1-136-B1 was chosen as a reference beam since it performed in a very typical manner. The max force that it could bear as well as failure displacement and fracture phenomena was seen as representative behavior.

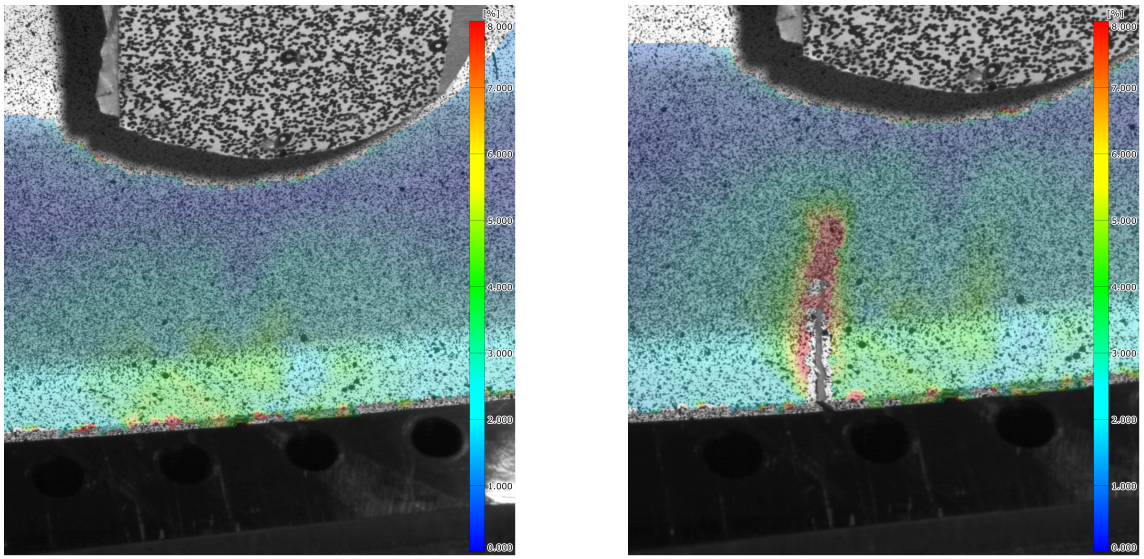

(a) Strain field, one timestep before crack initiation

(b) Strain field after crack propagation

Figure 4.33: DIC strain field data of beam *B1-136-B1*

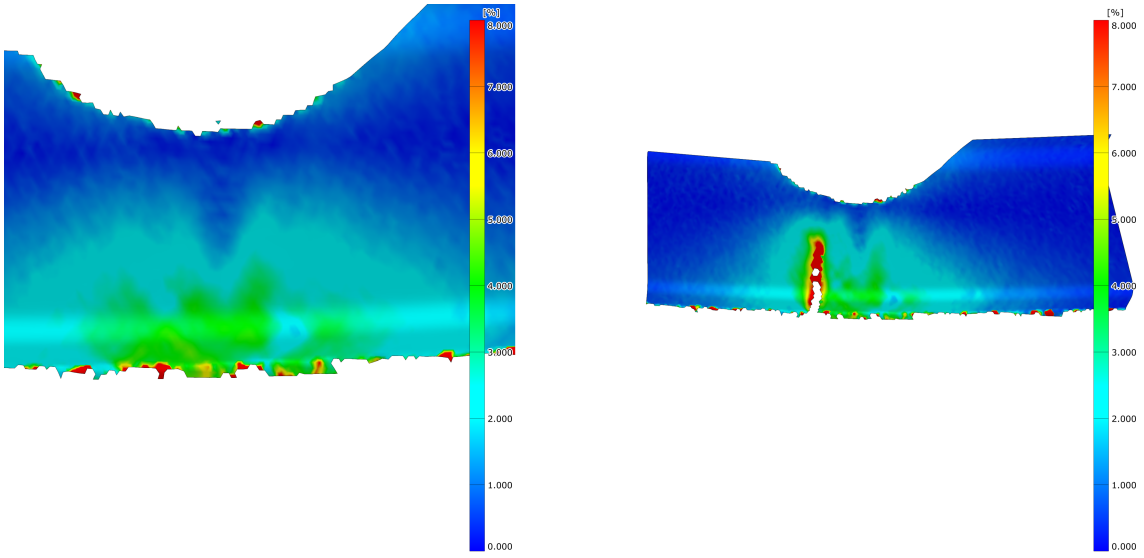

(a) Strain field, one timestep before crack initiation

(b) Strain field after crack propagation

Figure 4.34: 3D DIC strain field data of beam *B1-136-B1*

The three main metrics chosen for comparison characterize the crashworthiness of the component. Maximum force is a metric of the strength of the component, the failure displacement a measure of the overall ductility until the first fracture and the energy absorption is a way of taking into account sort of the whole failure process from hardening to final fracture. The standard deviation of the physical data is also taken into account to get a reference for how scatter impacts the overall reliability of the part. Firstly, the failure displacement for all simulations fall within the range

of the physical testing, albeit on average too high and only one of them fall within the standard deviation. The material card MAT16564 with the removed rib had the lowest force deviation from the mean and also follows the hardening curve most closely out of any simulation. The homogeneously scaled MAT16351 card has the lowest energy error although it can be seen graphically that if HEXAMAT16564 and PMM with MAT16564 had slightly lower failure strain they would perform much better in this metric. The baseline 3.4 mm MAT16351 card is overestimating the energy absorbed and is overpredicting the crashworthiness of this cast aluminium alloy. As a final note on these simulations, since all of the benchmark simulations from Figure 4.8 had extremely high overpredicting hardening curves, the greatest emphasis on this investigation was placed on first finding the cause to this. Therefore, what happens right after the first fracture was deemed a secondary goal for the simulations. Now that the results are closer in hardening nature it is clear that the failure phenomena are not quite the same, where it would be most accurate if there were more clear failure points, i.e, force dips. In the physical data it is generally understood that the first dip in the force corresponds to the first flange failing and the second dip is the second failing, but this was not definitively seen in the simulations.

It should be pointed out that the strain fields from the simulations also give a further indication to that it is the hardening of the material that is being overestimated, not necessarily the failure strain. The simulation data from Figure 4.32 should be compared to the DIC data from Figure 4.33 (or equally Figure 4.34). The qualitative nature of the strain fields in the simulations is similar and the DIC data, where there seems to be highest magnitude of strain in the flange in the middle of the beam that dissipates in a sort of 'M' shape. From the DIC it is seen that right before fracture the strain is around 5-6% while fracture itself occurs at around 8-10%. The simulation that came closest to this behavior is arguably the 2.0mm TETRA 0.7 homogeneous scaling of material card MAT16351, while the rest of the simulations give slightly too high predicted strain before fracture. But this is at most 1-2 percentage units.

4.6 Tensile test material validation

Simulated tensile tests showing engineering stress and strain are presented in Figure 4.35.

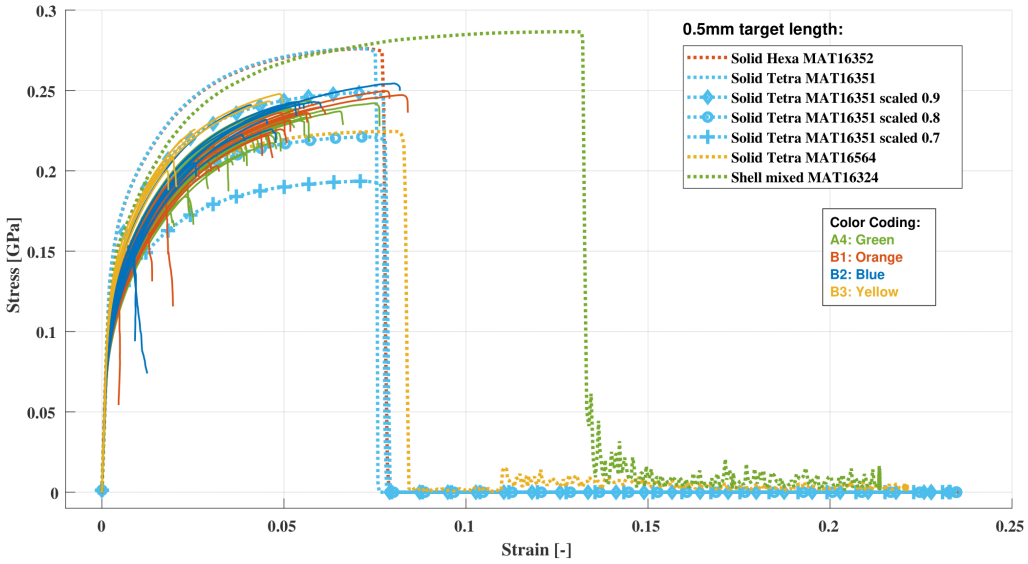

Figure 4.35: Tensile test: physical data vs. different material cards and scaling

Physical tensile test results provided by parallel thesis work [19] is compared with simulations of the material cards used in the investigation in Figure 4.35. The physical tensile tests were color coded based on the aluminium alloy batch which is the same identification as in the 'alloy abbreviation' column in table 3.1. On this level of comparison there are fewer variables that could cause scatter, for instance there are no critical load bearing parts for a simple coupon test nor significant stress concentration points. It is therefore quite surprising to see a high level of scatter for the failure strain. Furthermore there does not seem to be a definitive differentiation between the alloys when it comes to hardening and failure strain. This level of scatter was also seen for the three point bend test. It could be argued that the *B3* test sample performed better than average and that the *A4* tests performed slightly worse. However all the *B3* samples were taken from the same casting component of *snaketool 1.5* namely casting sample *B3-176*. Since they were all sampled from a single casting there is no statistical evidence to support that claim. It is, nevertheless, indicative that slight changes in the casting parameters between batches is causing more discernible difference in the results than the actual batch types. This is probably also causing the scatter in results for the beams subjected to three point bending.

As for the correlation between physical data and simulated results, it should first be noted that the shell material card MAT16324 massively overestimates the ductility of the material and this was also seen for the three point bending test. The solids did a much better job of predicting failure strain in both the three point bend and the tensile test although still on the side of overestimating the physical results. For the tensile tests the tetrahedral elements are performing just as well as the hexahedral elements. MAT16564 (which has applied scatter) is underestimating the hardening and strength of the material while it *overestimated* the strength of the aluminium in the component level test. Furthermore when the homogeneous scaling was applied to reduce the hardening of MAT16351 by 30%, the simulated results also underestimated the strength for tensile tests. The same scaling on the

component level, however, aligned very well with the results. For the tensile tests, scaling MAT16351 instead down by 10% resulted in the best alignment and one would have to scale down by 20% to achieve the same results as the scatter card MAT16564. In other words, it seems that for some reason the material cards are performing worse for the three point bend test than the tensile test.

5
Conclusions

Three point bending tests of the component show little sensitivity to increased levels of iron and vanadium in the alloy, as well as to wether it has been paint-baked or not.
Simulations show small sensitivity to what type of elements that are used, as long as it is not shell elements.
By employing scaling and altering the geometry supported by findings in three point bend testing as well as CT-scanning the error was reduced to within one standard-deviation of the test results. This echoes previous findings at VCC that also suggest scaling is necessary to achieve good correlation in HPDC component testing.
Concerning porosity, the potential negative impact on material stiffness could not be entirely captured by any of the methods employed in this work. Other potential methods for capturing porosity are discussed in the mapping section, 5.4. The discrepancy between the PMM and CTM further suggests that an imperfection other than porosity causes the over-stiff CAE models.
Comparing CAE with tensile test results suggests the calibrated material model MAT16351 being too stiff. Here scaling with 0.9 gives comparable results. In contrast to this the component simulations achieved best accuracy with scaling by 0.7. This points to that a phenomenon more present in the beam than in the snaketool flats causes a greater reduction in stiffness. This (or some other phenomenon) is also higher in the snaketool than in the softfloor, for which the MAT16351 was calibrated. This raises questions about how reliable the material testing and calibration, and verification actually is and, again, what phenomenon in the megacasting that is causing the reduced material properties of the aluminum.
Whether porosity contributes to the spread in testing results is hard to comment on since only one beam was scanned and differences in porosity is hard to quantify from fracture surfaces.

5.1 Physical testing

Despite being very intricate and methodical with the physical testing, quite a lot of spread was observed in the results. No clear distinction can be made between the alloy batches and the spread within the batches is bigger than between the alloys. One obvious outlier can be seen in the testing results, namely *B2-150*. It is an outlier both when it comes to strain until failure, and the failure mode. Another aspect, further emphasizing the unpredictability is that the two best performing specimens, *B1-130* and *B1-135*, are not made from primary alloy.

Surface imperfections such as the dents from the ejector pins could have influenced experimental results by introducing for example stress concentrations in the flange. Such imperfections further emphasize issues with the manufacturing process and possible increased spread in the experimental results.

Regarding the slightly higher hardening of the *B3-176-B1* specimen, it is worth noting that both the beam and all the tensile tests with this alloy come from the same casting (#176 in the sequence). This further increases the likelihood of this being a statistical outlier or cause of other circumstances rather than actual material characteristic. It is however interesting that the alloy with increased iron and vanadium content is at least on par with the purer alloys.

5.1.1 CT-scanning

From the three point bend of the *A4*-102-B1*-beam, conclusions can be made that the flange depth, the milled features and paint baking did not severely impact the load bearing capacity of the beams. In other words, the CT-scanned beam was deemed representative of the general porosity of the other tested beams. From the CT-scan, it is clear that the cast beams have high levels of porosity; on average around 1% of the material was found to be void when a refined CT scan was conducted. CT-scanning could be explored further, for example the beam could be subjected to bending until plasticized and thereafter scanned again, or scanned after three-point-bend until total failure. This would give another dimension to how porosity might develop during loading and deformation.

5.2 Hexahedral mesh

From studies on hexahedral elements, several conclusions can be drawn. The lower stiffness exhibited by hexahedral elements suggests they show exhibit less shear locking than tetrahedral elements. This applies to both material models MAT16351 and MAT16564.
Given the complications associated with creating a hexahedral mesh for a complicated part, both the ease at which the *TETRA2HEXA* mesh was created, and the performance of the same is promising. The implications of this is that one could avoid the issues of shear locking quite effectively by creating a coarse tetra mesh and use the tetrahedron to hexahedral function, thus achieving a hexahedral mesh in a fraction of the time and effort it would have taken to create a high quality hexahedral mesh manually.

5.3 Solid vs Shell

Shell modeling makes very much sense when working with sheet metal due to both the reduced number of elements and therefore higher efficiency. But this higher

efficiency is harder to motivate when the result is so far from what is achieved with solid elements and is exhibited in physical testing.

As is evident in both the initial simulations as well as in the subsequent geometry and mesh refinement studies, the shell elements cannot predict the behavior of the cast beam very well. The force-displacement response in the mesh sensitivity study does not at all converge in the same way as the solid tetra elements. Not much happens when refining the mesh beyond 2.5 mm, which is an indication that convergence has been achieved. Additionally, shell elements are more sensitive to initial conditions and configuration, as made clear from the geometry study.

5.4 Mapping

5.4.1 Micro-mapping: CTM and PSDM

PSDM mapping was limited by potentially erroneous input-data from the casting simulations, but an architecture has been set up which might aid in the future when the accuracy of the simulations has been improved. Refining the resolution of the CT scan proved to capture more pores and get a better representation of the reduction in failure strain and hardening. Both of the mapping techniques failed to fully account for the discrepancy between physical testing and simulated results. It should be noted that it was argued that the middle-rib was particularly porous but that the CT scans did not pick up on this. Furthermore, simulations in *ProCast* do not account for the evaporating release agent that could have caused trapped gas in the rib. In other words, it is still unclear why the middle rib looked the way it did on the fractography in Figure 4.4 and why the CT scans did not pick up on it, even with very high resolution. This is again a sign that a phenomenon other than porosity is what is causing the reduced strength in the material.

5.4.2 Porosity meshing

For MAT16564 the results were non-physical while for MAT16351 it resulted in a moderate drop in hardening and failure strain. A theory behind why MAT16564 behaved this way could potentially be time control issues due to the very fine elements or that scaling is applied to a mesh that already accounts for porosity, so one is essentially accounting for adverse effects twice. In either case, it's hard to conclude that improvements were made to the model since the pores themselves had to take on different volumes and geometries in order to be simulated since it would be impossible to simulate at the refinement needed for the original scans. Since no ground breaking improvements to the model were made here it is therefore hard to justify this method of mapping the CT scan to the model considering the added computational cost, not to mention the time investment in scanning the part in the first place.

5.4.3 Hardening curve- and homogeneous scaling

The scaled hardening curves produced were generally in agreement with the RVE material behavior. It was further seen that the RVE scaling performed in this investigation had a generally good agreement with results produced by Coric and Seyedraoufi [1] and a overlap with studies done for cross section surface void fractions [21]. However the approach did not transfer very well to the component level for the three point bending tests. Upon validation with physical and simulated results from the tensile test, it was shown that scaling down the material card homogeneously by 10% resulted in satisfactory behavior, meanwhile the hardening in the component simulation had to be scaled by 30% for good alignment. This indicates that the porosity in the beam or in regions of the beam that are critical have a higher level of porosity than the flats from where the tensile tests were sampled from. In this aspect it would be interesting to also have CT-scanned the specimens used in tensile testing to investigate if there is a difference in porosity in the different sections of the beam which might explain the difference in material properties.

5.5 IGA

We can draw the conclusion from the geometry mesh study that as long as the mesh captures the geometry the mesh doesn't really matter and can be quite coarse. A less complicated part could most likely be meshed with a much finer mesh and vice versa. It is also possible that the mesh could be refined locally, to capture local regions that need higher resolution. The loading time for the geometry mesh is negligible compared to the time required to generate the background mesh and perform the simulation, so the benefit of having a coarse mesh is not that great.
When it comes to element edge length, there seems to be a higher dependency. The most accurate is still the 2 mm EEL. Interestingly, unlike the geometry mesh and the FEM meshes, the smallest one doesn't perform the best with 2 mm one outperforming the 1 mm.
DYNA has during their own research determined that one can use a background mesh that has a element length four times as large as the FEM mesh for the same problem and achieve the same results. This is however not something that has been observed in this study.
IGA shows great promise as a future modeling tool. Given its recent development, calculations can certainly be made more efficient, and the process can be parallelized further, significantly reducing runtime. The failure mechanisms also need calibration, as IGA does not yet capture or visualize the same failure behavior seen in both FEM and physical testing. Currently and in the near future, it may serve as a verification tool or provide corroborative insight to traditional FEA.

5.6 Recommendations for future research

Since the test specimen pool didn't include any beams from position B2 in the snake tool the ability to investigate the effect of flow length was limited.

As can become evident in for instance application of neural networks, overfitting can very quickly become a problem. Its hard to know if simulation "improvements" are actually improving performance or just make the results closer to the experimental results. Therefore, a second type of test for (for validation) investigating a different type of loading scenario would be useful to reduce the risk of overfitting, or evaluate how much overfit is present. A suitable type of test would for example be an axial crush type of test. Furthermore, if scatter is reduced between casting trials, it could be prudent to test on a much larger sample size on a component level to avoid overfitting.
The physical test results exhibited too much spread between castings to conclude if there is a difference in performance in the different type of alloys. Once the spread between castings has been reduced it may be feasible to investigate the effect of deviations in iron and vanadium content from the primary alloy on the mechanical properties.
Making further mapping modifications to the model can be explored especially for GISSMO since the the incremental damage evolution in this model is meant to represent the nucleation, growth and coalescence of voids. Pores and imperfections as a result of the casting process could be used to map porosity to a pre-damage variable so that some elements will have $D > 0$ before the start of the simulation. The benefit of doing so is that the evolution of the pores are in some way captured. By simply scaling hardening and strain, there is no accounting for how the pores grow and deform under stress but perhaps the damage evolution model could come closer to modeling this phenomena. For reference, porosity modeling has been investigated since the mid 1970's where the Gurson-Tvergaard-Needleman (GTN) model was first developed [24]. The GTN model is also a damage evolution model but very distinct from GISSMO. This could also be investigated, however given VCCs experience with GISSMO it makes more sense to first investigate this avenue before alternative methods of modeling porosity are explored.

Bibliography

[1] Coric, B., & Seyedraoufi, S. (2024). The Effect of Pore Geometry on the Mechanical Properties of Cast Aluminium. Master's thesis, Chalmers University of Technology, Gothenburg, Sweden. Department of Industrial and Materials Science.

[2] Shreedhara, S. V., & Singh, S. R. (2019). CAE modelling of cast aluminium in automotive structures. Master's thesis, Linköping University, Department of Management and Engineering. Linköping University Electronic Press.

[3] Al-Karawi, O., & Mathiesen, V. (2024). Verification of plane stress material model behaviour in solid 3D-structures. Master's thesis, Chalmers University of Technology, Department of Industrial and Materials Science.

[4] Olofsson, J., & Svensson, I. L. (2013). Closed chain simulations of a cast aluminium component: Incorporating casting process simulation and local material characterization into stress-strain simulations. Jönköping University, School of Engineering, Department of Mechanical Engineering, Materials and Manufacturing – Casting.

[5] Slota, J., Gajdos, I., Jachowicz, T., Siser, M., & Krasinskyi, V. (2015). FEM simulation of deep drawing process of aluminium alloys. Applied Computer Science, 11(4), 7–19.

[6] Tiryakioglu, M., Campbell, J., & Nyahumwa, C. (2011). Fracture surface facets and fatigue life potential of castings. Metallurgical and Materials Transactions B, 42(2), 341–347. doi:10.1007/s11663-011-9577-3.

[7] Henriksson, F., & Johansen, K. (2016). On material substitution in automotive BIWs – From steel to aluminum body sides. In Proceedings of the 26th CIRP Design Conference (pp. 123–130). Elsevier B.V. doi:10.1016/j.procir.2016.05.028.

[8] Tisza, M., & Czinege, I. (2018). Comparative study of the application of steels and aluminium in lightweight production of automotive parts. International Journal of Lightweight Materials and Manufacture, 1(3), 229–238. doi:10.1016/j.ijlmm.2018.09.001.

[9] Rahmat, M. (2019). Dynamic mechanical characterization of aluminum: Analysis of strain-rate-dependent behavior. Mechanics of Time-Dependent Materials, 23(4), 385–405. doi:10.1007/s11043-018-9393-0.

[10] Bai, Y., & Wierzbicki, T. (2008). A new model of metal plasticity and fracture with pressure and Lode dependence. *International Journal of Plasticity, 24*(6), 1071–1096.

[11] Basaran, M. (2011). Stress State Dependent Damage Modeling with a Focus on Lode Angle Influence. PhD Thesis, RWTH Aachen University, July. ISBN: 978-3-8440-0446-5.

[12] LSTC (2002). LS-DYNA Theory Manual, Retrieved from `https://ftp.lstc.com/anonymous/outgoing/web/ls-dyna_manuals/DRAFT/DRAFT_Theory.pdf`

[13] Zhang, Y., & Shen, F., & Zheng, J., & Münstermann, S., & Li, T., & Han, W., & Huang, S. (2022). Ductility prediction of HPDC aluminum alloy using a probabilistic ductile fracture model. *Theoretical and Applied Fracture Mechanics. Volume 119, 2022, 103381, ISSN 0167-8442,* `https://doi.org/10.1016/j.tafmec.2022.103381`

[14] Zhai, Q., & Tang, R., & Zhu, P., & Liu, Z. (2025). A novel method for predicting mechanical properties of megacasting alloy based on the modified GTN model and machine learning. *Engineering Failure Analysis, Volume 174, 109536, ISSN 1350-6307,* `https://doi.org/10.1016/j.engfailanal.2025.109536.`

[15] Hultmark, A. H. (2025). Email regarding findings during fracture surface examination. Personal communication, received on March 6, 2025.

[16] LSDYNA LSTC (2025). LS-DYNA Theory Manua. Accessed 2025-03-28, 2025-05-08, 2025-05-15. `https://ftp.lstc.com/anonymous/outgoing/web/ls-dyna_manuals/DRAFT/DRAFT_Theory.pdf`

[17] N. Ottosen and M. Ristinmaa (2005), *The mechanics of constitutive modeling*, London, England. Elsevier Science. https://doi.org/10.1016/B978-0-08-044606-6.X5000-0

[18] M. Jolly, L. Katgerman (2022), *Modelling of defects in aluminium cast products*, Progress in Materials Science, Volume 123, 100824. https://doi.org/10.1016/j.pmatsci.2021.100824

[19] Teja B.M., N. & Yang, J. (2025). Mechanical Performance and Material Characterization of Secondary Aluminum Alloys for Megacasting. Master's thesis, Chalmers University of Technology, Gothenburg, Sweden. Department of Industrial and Materials Science.

[20] E. Lordan Y. Zhang, K. Dou, et al.(2021), "On the probabilistic nature of high pressure die casting," Materials Science and Engineering: A, vol. 817, p. 141 391, 2021, issn: 0921-5093. doi: https : / / doi . org / 10 . 1016 / j . msea . 2021 . 141391. [Online]. Available: https://www.sciencedirect.com/science/article/pii/S0921509321006602.

[21] C. Cáceres & B. Selling, "Casting defects and the tensile properties of an alsimg alloy," Materials Science and Engineering: A, vol. 220, no. 1,

pp. 109–116, 1996, issn: 0921-5093. doi: https://doi.org/10.1016/S0921-5093(96) 10433-0. [Online]. Available: https://www.sciencedirect.com/science/article/pii/S0921509396104330.

[22] M, Montari, L. Liping, N. Petrinic (2017). Isogeometric models for impact analysis with LS-Dyna. 11th European LS-Dyna conference, Salzburg, Austria.

[23] D. Mohr (2015) *Ductile fracture, theory and experiments*. Lecture 8, ETH Zurich, Department of Mechanical and Process Engineering, Chair of Computational Modeling of Materials and Manufacturing.

[24] Jun Zhou, Xiaosheng Gao, Jabes C. Sobotka, Bryan A. Webler, Brian V. Cockeram (2014). On the extension of the Gurson-type porous plasticity models for prediction of ductile fracture under shear-dominated conditions. *International Journal of Solids and Structures*, Volume 51, Issue 18, Pages 3273-3291. Available: https://doi.org/10.1016/j.ijsolstr.2014.05.028.

[25] Helmut Gese, Gernot Oberhofer (2018). Material parameter identification for MF GenYld + CrachFEM - Metallic materials

[26] André Haufe, Paul DuBois, Frieder Neukamm, Markus Feucht (2011). GISSMO - Material Modeling with a sophisticated Failure Criteria. LS-Dyna Developer Forum 2011, Dynamore - Stuttgart - A. Haufe. Available: https://www.dynamore.de/de/download/papers/forum11/entwicklerforum-2011/haufe-gissmo.pdf

A

Beam Anatomy

To more effectively reference the beam anatomy, the different regions of the beam have been numbered. The numbering can be seen in figure A.1 or the more zoomed in A.2 as well as A.3. This nomenclature will mainly be used when describing the fracture evolution, but also for more accurate descriptions. The nomenclature is presented in table A.1.

Table A.1: Beam anatomy

1	Flange on converging side / A-side
2	Converging rib
3	Center / middle rib
4	Flange on diverging side / B-side
5	Ejector pin
6	Flat
7	Roof
$1 \cup 6 \cup 7 \cup 4$	U-profile / Hat shape

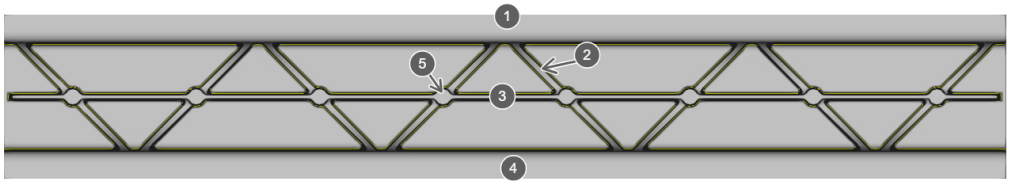

Figure A.1: Beam with numbered regions

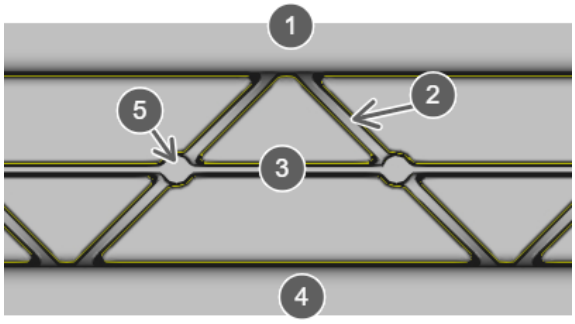

Figure A.2: Beam from below with numbered regions

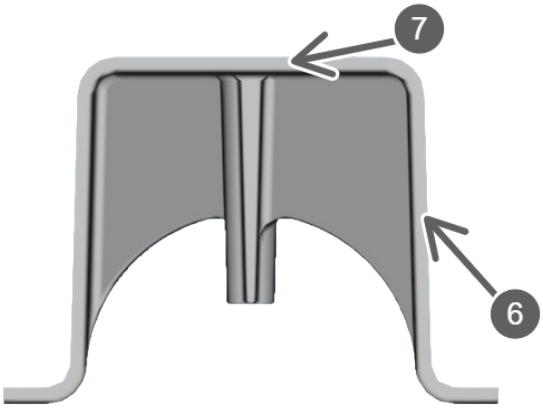

Figure A.3: Beam in profile with numbered regions

B

Three point bend of CT-scanned beam

The comparison between the previous test results and *A4*-102-B1* is shown in figure B.1.

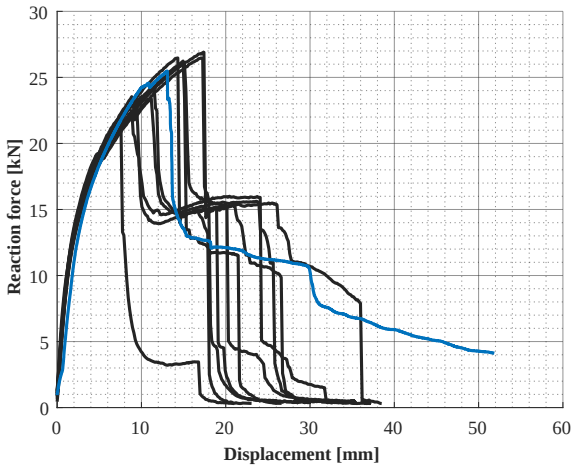

Figure B.1: Comparison between force-displacement curves, scanned beam shown in blue

The *A4*-102-B1* beam post-experiment is shown in figure B.2.

(a) *A4*-102-B1*, viewed from A-side **(b)** *A4*-102-B1*, viewed from B-side

Figure B.2: *A4*-102-B1* post three-point bend test

Given all the things that pointed to that the *A4*-102-B1* beam might give different force-displacement behavior it performed on par with the other test specimens. It showed very comparable force against displacement in both the linear and hardening regions, as well as had a similar displacement and force at the first failure. It should be noted that the behavior after the first failure of the *A* flange and side is not

typical. The beam manifested a failure sequence not before observed where the *B*-side did not fail and the beam instead capsized and was bending in a was which was not intended.

C

Statistical tools

Outlier Detection Methods

Interquartile Range (IQR)

$$
\begin{aligned}
Q1 &= \text{median of the first half of the data} \\
Q3 &= \text{median of the second half of the data} \\
\text{IQR} &= Q3 - Q1 \\
X < Q1 - 1.5 \times \text{IQR} \quad &\text{or} \quad X > Q3 + 1.5 \times \text{IQR} \quad \text{(Outlier)}
\end{aligned}
$$

Z-Score

$$
\begin{aligned}
Z &= \frac{X - \mu}{\sigma} \\
|Z| &> 3 \quad \text{(Outlier)}
\end{aligned}
$$

Modified Z-Score

$$
\begin{aligned}
Z &= 0.6745 \times \frac{X - \text{median}}{\text{MAD}} \\
|Z| &> 3.5 \quad \text{(Outlier)}
\end{aligned}
$$

Dixon's Q Test

$$
\begin{aligned}
Q &= \frac{|x_a - x_b|}{R} \\
Q &> \text{critical value} \quad \text{(Outlier)}
\end{aligned}
$$

Analysing Hardening curves

For every simulated point, a range of $\pm 0.2mm$ is defined such that the physical testing curve for each point is sampled around the relevant displacement. This range is visualized for each point in C.1 to make it easy to see which testing points are sampled to make a cluster. This is done because the testing data is of course

sampled at a different interval than the simulated points. After taking out this sample of points on the testings curve, one is left with a cluster of points of roughly equal displacement values. This cluster of test points now has a defined median and MAD that can be used for the modified Z-score. Alternatively one could have used other statistical tools on these clusters but for this investigation the modified z-score was used.

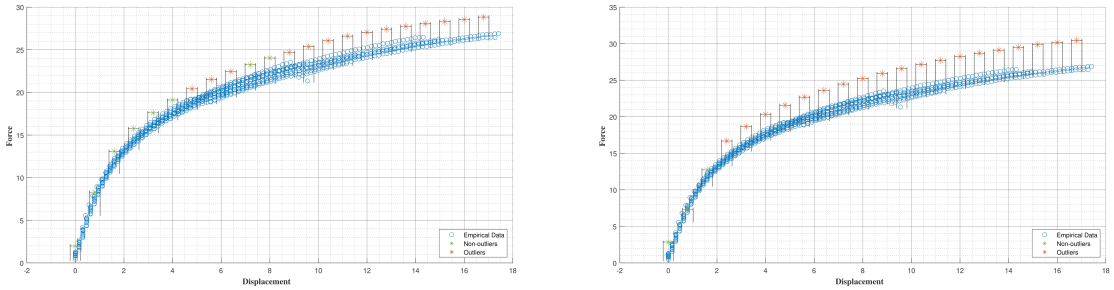

(a) HEXA MAT16564, statistical outliers

(b) TETRA MAT16564, statistical outliers

Figure C.1: Finding statistical outliers for hardening curves

DEPARTMENT OF SOME SUBJECT OR TECHNOLOGY
CHALMERS UNIVERSITY OF TECHNOLOGY
Gothenburg, Sweden
www.chalmers.se

CHALMERS
UNIVERSITY OF TECHNOLOGY